Visibility stacking with MeerKAT: opportunities and pitfalls

By

Thato Eugine MANAMELA

UNIVERSITEIT VAN PRETORIA
UNIVERSITY OF PRETORIA
YUNIBESITHI YA PRETORIA
Denkleiers • Leading Minds • Dikgopolo tša Dihlalefi

Department of Physics
UNIVERSITY OF PRETORIA

Submitted in partial fulfilment of the requirements for the degree of MASTER OF SCIENCE (MSC) IN PHYSICS in the Faculty of Natural and Agricultural Sciences.

December 15, 2020

Supervisor: Prof. Roger DEANE

Go hlakantšha diponagalo ka thelesekopo ya MeerKAT: menyetla le mathata

Mongwadi

Thato Eugine MANAMELA

UNIVERSITEIT VAN PRETORIA
UNIVERSITY OF PRETORIA
YUNIBESITHI YA PRETORIA
Denkleiers • Leading Minds • Dikgopolo tša Dihlalefi

Lefapha lab Thuto ya Fisika
YUNIBESITHI YA PRETORIA

Thesisi ye ngwadilwe ka tshwanelo ya tikree ya MSc wa fikisika mo lekala la thuto ya Thutamahlale ya Tlhago le Temo.

Manthole 15, 2020

Mookamedi: Prof. Roger DEANE

UNIVERSITY OF PRETORIA

Abstract

Faculty of Natural and Agricultural Sciences
Department of Physics

Master of Science (MSc) in Physics

Visibility stacking with MeerKAT: opportunities and pitfalls

by Thato Eugine MANAMELA

Supervisor: Prof. Roger DEANE

Stacking is a statistical approach to measure the average properties for known objects that are too faint to be detected individually at the target wavelength. This approach has been extensively used for studies of high redshift, and/or intrinsically faint galaxies with a wide range of telescopes, including radio inteferometers. The technique is typically applied using images rather than the direct measurement of an interferometer, namely Fourier components of the sky brightness distribution. However, interferometry is not a direct imaging method, and this imposes several challenges to stacking, limiting scientific inference. This thesis tests where visibility stacking might be more effective than the traditional image-plane stacking approach using simulated data, as well as real observations from the MeerKAT telescope. To do so, we perform a suite of visibility stacking experiments on realistic synthetic data generated from the TRECS Square Kilometre Array simulations. Parameters that are varied include the CLEAN depth, stacking depth and the maximum source distance from the phase centre. We further investigate the applications of visibility stacking on real MeerKAT data. The stacking techniques are applied on HI-selected galaxies within the Abell 3408 galaxy cluster. Our simulated and real data results suggest that visibility stacking produces favourable results compared to image-stacking for shallow observations, but caution must be applied to sub-μJy stacked sensitivity experiments.

Declaration of Authorship

I, Thato Eugine MANAMELA, declare that the thesis, which I hereby submit for the degree of MSc in Physics at the University of Pretoria, is my own work and has not previously been submitted by me for a degree at this or any other tertiary institution.

Signature: _____

Date: _____

Acknowledgements

- Firstly I would like to thank my supervisor, Prof. Roger Deane, for his guidance through each stage of the process. Thank you, Roger.
- Thanks to Prof. Oleg Smirnov and the ILIFU team for helping out during the stressful technical difficulty times.
- This thesis used data from the MeerKAT telescope, which is operated by the South African Radio Astronomy Observatory, which is a facility of the National Research Foundation, an agency of the Department of Science and Innovation.
- Thanks to the UP Astro group for their support.
- We acknowledge the use of computing facilities of the Inter-University Institute for Data Intensive Astronomy (IDIA) for this work. IDIA is a partnership of the Universities of Cape Town, of the Western Cape and of Pretoria.
- I would like to acknowledge the National Astrophysics and Space Science Programme (NASSP) and the National Research Foundation (NRF) for funding.
- My family and friends for their love and support.

Contents

List of Figures

List of Tables

Chapter 1

Introduction

In this first chapter, we provide a brief introduction of radio astronomy and how radio signals are interpreted once reaching our radio instruments, we then describe the dominant extragalactic source populations in the faint radio sky. Lastly, we give an introduction to radio interferometry as relevant to this thesis.

1.1 Radio Astronomy

Celestial objects emit light in different parts of the electromagnetic (EM) spectrum, one example being radio light which ranges in wavelength from about 1 centimetre to 10 metres on the EM spectrum. EM light or radiation travels at the speed of light $c \approx 3 \times 10^8$ ms^{-1} in a vacuum and one can interchange between wavelength and frequency using the relation:

$$c = \nu\lambda, \tag{1.1}$$

where ν is the frequency in units of Hertz and λ the wavelength in metres. Radio astronomy is the study of celestial objects emitting at the radio regime of the electromagnetic spectrum. The first detection of cosmic radio emission was serendipitously observed by Karl Jansky in 1933 at the Bell Telephone Laboratories in Holmdel, and the detection came from the centre of the Milky Way (Jansky, 1933). This discovery later led to the development of radio astronomy. However, only radio, infrared and visible light observations are typically performed from Earth, while other wavelengths or frequencies being obscured by the Earth's atmosphere, requiring their observations to either be in space or high, dry sites (Marr, Snell, and Kurtz, 2015). Radio emission is detected using radio telescopes (also referred to as radio antennas) and can either be used as a single antenna or linking multiple receptors by applying the radio interferometry technique (e.g., Müller and Peichl, 1991). Using multiple antennas and correlating the outputs of the individual receivers allow to achieve a better angular resolution than using a single antenna, this concept will be discussed briefly in Section 1.2.2.

Astronomers study the physical or chemical properties of celestial sources through EM radiation. This requires a deep understanding of how it interacts with the earth's atmosphere before reaching our telescopes, also how the measurement itself and our telescopes interfere with the signal. If we assume a light radiating source being observed, the light energy emitted by the source falling on a radio telescope can be described in terms of spectral brightness (also referred to as spectral intensity) I_ν measured in W m^{-2} Hz^{-1} sr^{-1}. The resulting flux density or just flux of the telescope is defined as

$$S_\nu = \int_{source} I_\nu(\theta, \phi), \tag{1.2}$$

and units for S_ν are W m^{-2} Hz^{-1} and are normally expressed in Jansky, where 1 Jansky (1 Jy) is equivalent to 10^{-26} W m^{-2} Hz^{-1} (Condon and Ransom, 2016). The spectral brightness can not be precisely measured if the observed source is unresolved (small in angular size relative to the angular resolution of the telescope). Therefore very faint and distant sources can only be measured in terms of flux density if a telescope does not have the required angular resolution.

1.1.1 Radiation Mechanisms

The most common way to understand underlying physical EM radiation mechanisms is to measure how the radiation intensity varies with frequency (i.e., spectral emission distribution or spectra), simple example illustrations of spectra are shown in Figure 1.1. Radiation mechanisms can generate a spectral-line (which can be in the form of absorption, emission or broadened) or continuum spectra. A continuum spectrum is due from a wide frequency range observations while spectral-line is due from narrow frequency range observations.

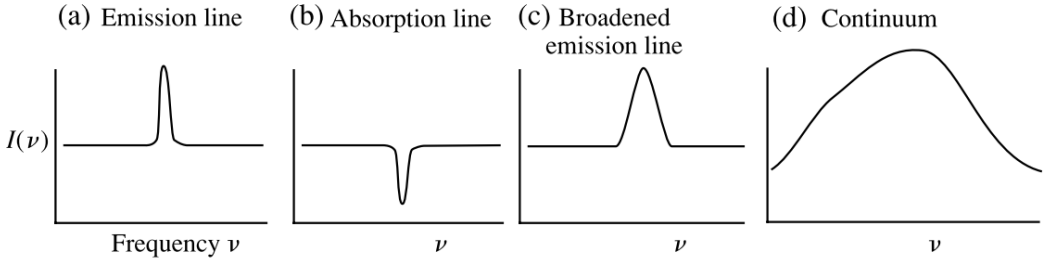

FIGURE 1.1: Simple examples of spectra. Image is directly reproduced from Bradt (2004).

A continuum spectrum can be produced by two different processes, namely thermal radiation, where energy is in the form of heat or synchrotron radiation where energy is non-thermal. Each of the processes has different signatures on the spectral emission distribution (SED) and tells different physical processes about a source. For example, if you measure a spectrum where the specific intensity or flux density increases with temperature, then the mechanism taking place is of thermal radiation defined by the Plank's function in Equation 1.3, where the I_ν is the measured intensity observed at frequency ν, h is the Plank's constant, c is the speed of light in a vacuum, K_B is the Boltzmann constant and T is the brightness temperature of the observed source in thermal equilibrium. If the specific intensity decreases with frequency, then it is mostly likely to be synchrotron radiation (King, 2015). This thesis will be mainly focused on sources that emit synchrotron radiation.

$$I_\nu = \frac{2h\nu^3}{c}\frac{1}{e^{\frac{h\nu}{k_B T}} - 1} \quad [Wm^{-2}Hz^{-1}sr^{-1}] \tag{1.3}$$

Synchrotron radiation occurs when electrons spiral around magnetic field lines due to the non-relativistic magnetic force $F = q\nu \times B$, where q is the charge of an electron moving with speed v in magnetic field strength B. Since the electrons are relativistic, the emitted radiation becomes so intense that it can reach to high energies such as X-rays and γ-rays. Synchrotron radiation can also be detected in radio due to being the strongest at low frequencies. The spectrum of synchrotron radiation can be represented by a power law of the form:

$$S_\nu \propto \nu^{-\alpha}, \tag{1.4}$$

where S_ν is the flux density measured at observational frequency ν, α is the spectral index (Bradt, 2004). Figure 1.2 illustrates spectra examples of synchrotron sources and radio galaxies in the literature.

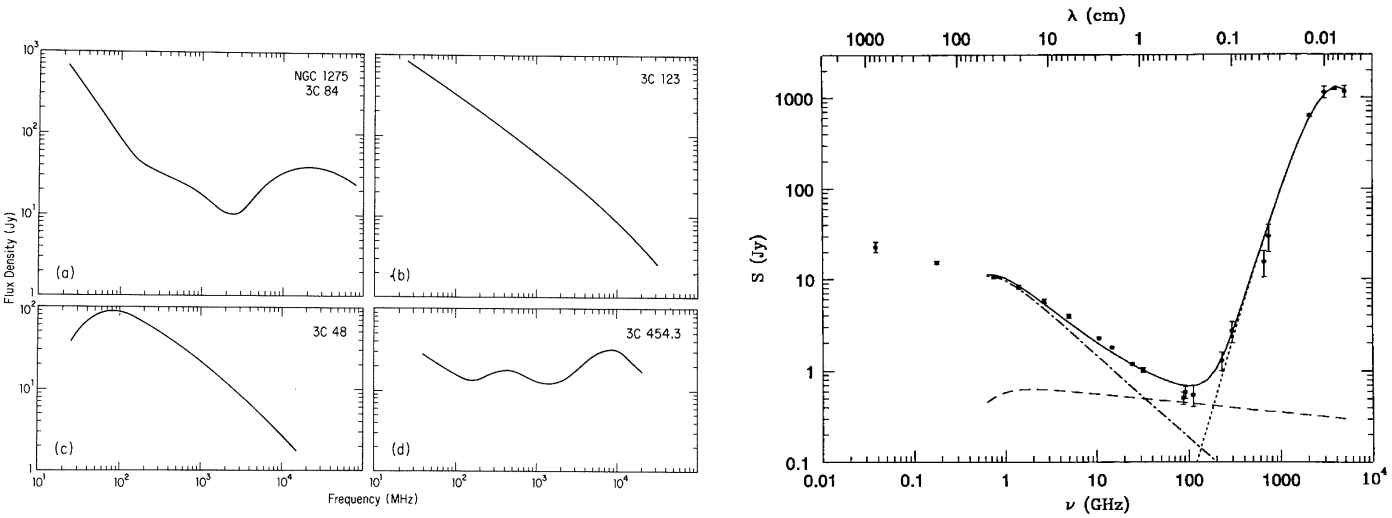

FIGURE 1.2: **Left panel**: spectra of radio galaxies (top panels), radio source 3C 84 hosted in galaxy NGC 1275 contains a compact nuclear component that is opaque below about 20 GHz, while 3C 123 is transparent at all frequencies and loses energy making the spectrum steep at fewer GHz; and quasars (bottom panels), 3C 48 at below 100 MHz it is synchrotron self-absorbed, while 3C 454.3 contains structures of different sizes that become opaque at different frequencies. **Right panel**: infra-red and radio spectrum of a starburst galaxy M82, the slightly horizontal dashed line indicates the contribution from free-free emission, the dots indicate thermal dust at low and high frequencies, respectively, the dot-dash line curve indicates synchrotron radiation. The free-free emission absorbs some of the synchrotron photons and flattens the overall spectrum at the lowest frequencies. Images are directly reproduced from Condon and Ransom (2016).

1.1.2 Radio Source Populations

The extragalactic radio sky is divided into the "bright" and "faint" radio sky population, where sources that fall under the bright radio sky are radio galaxies (RGs) and radio quasars, while sources that fall under the faint radio sky are radio-quiet active galactic nuclei (RQ AGN), Star-forming galaxies (SFGs) and FR 0 RGs (Padovani, 2016). For this thesis, the main focus will be on the faint radio sky population.

A physical structure of typical active galactic nuclei (AGN) includes a supermassive black hole (SMBH), an accretion disc emitting at optical/ultra-violet and X-ray radiation, fast moving gas clouds which appear as broad lines, slow moving gas clouds appearing as narrow lines on an AGN spectrum, the broad-line regions have velocity width in range 200 < Full width half maximum (FWHM) < 500 kms^{-1} (Groves, 2006), while the FWHM of the narrow line regions is in the range 5000 - 10000 kms^{-1} (Véron-Cetty and Véron, 2000). Also, the physical structure consists of a torus and high energetic-charged particles forming luminous jet and/or lobes

(Padovani, 2016). A cartoon example of an AGN physical structure is illustrated in Figure 1.3.

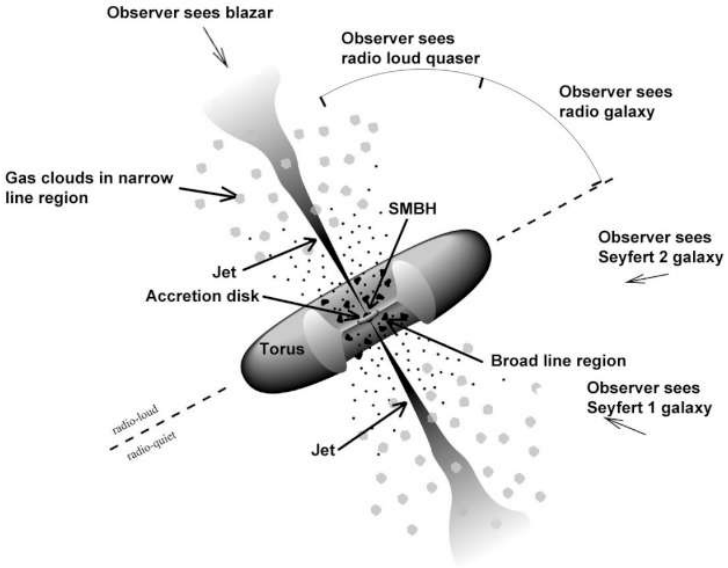

FIGURE 1.3: An illustration of an active galactic nuclei unification model, showing that the type of AGN class depends on the observer's viewing direction, where the types of AGNs observed are indicated with arrows. Image is directly reproduced from Condon and Ransom (2016).

Studies of AGNs have shown that there are two classes of AGNs which are classified in terms of their luminosity, radio-loud (RL) and RQ AGN, typical luminosities of RQ AGN are $L_{1.4GHz} \lesssim 10^{24}$ W Hz^{-1}, which is 10^3 less luminous than RL AGN. RL AGN are associated with large-scale jets and lobes, and also are mostly found in elliptical galaxies, while RQ have little or weak emitting ejecta and are found in spiral galaxies (Xu, Livio, and Baum, 1999; Wilson and Colbert, 1994). RQ AGN got their name from the fact that they were undetectable with radio telescopes of that time, and only to find out after the improvement of the sensitivity of radio telescopes that the sources are actually radio faint, but the radio-quiet name stuck (Sandage, 1965). In the context of this thesis, it is to note that RQ does not mean radio silent. The RQ AGN class dominates $> 90\%$ of the AGN family, making their studies more important when it comes to understanding the mysteries behind AGN and galaxy evolution, and can be divided into two classes, according to their optical spectra, (i) the type-I AGN, also called Seyfert 1 (Sy1), this class type shows both broad and narrow lines on an AGN spectrum and (ii) type-II AGN (Seyfert 2 or Sy2) show only narrow lines. Type I and II AGN are classified as radiative-mode sources. In contrast, jet-mode sources are AGN with low-ionisation nuclear emission-line regions (LINERs) (Heckman and Best, 2014), the schematic drawing of each respectively is shown in Figure 1.4, also see Figure 1.5 for their total energetic output, the Eddington distribution ratios.

The appearance of an AGN and its host galaxy are determined by the observer's viewing direction or viewing angle, because the radiation-emitting by the nuclei is not isotropic, and this effect is called the *Unification Model* (Barthel, 1989; Antonucci, 1993). For example, sources with jets along the viewing direction will have much brighter nucleus compared to sources with obscured jets. Another example is in

Figure 1.3, a cartoon illustration of a unification model of an AGN, where the broad-line region and jets are orientated close to the observer's viewing direction, giving the AGN a quasar or Sy1 galaxy appearance.

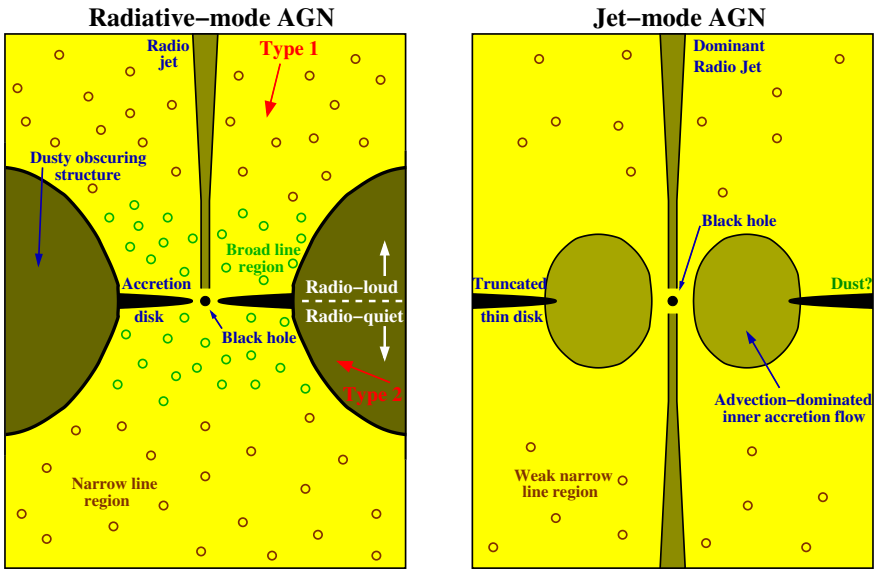

FIGURE 1.4: Radiative-mode and jet-mode AGN schematic diagrams. **Left panel**: radiative-mode AGN consists of a supermassive black hole (SMBH) that is surrounded by a geometrical thin and optically thick accretion disk. The dusty obscuring structure makes it difficult to view the SMBH, accretion disk and the broad-line regions, resulting in the AGN being observed as a type II, whereas at other lines of sight are not obscured and a type I AGN is observed. Jets can be produced in small proportions. **Right panel**: in jet-mode AGN the accretion disk is in the outer regions, replaced by the advance-dominated inner accretion flow. The majority of energy is released through radio jets in the form of Kinetics. Image is directly reproduced from Heckman and Best (2014).

SFGs are mostly associated with spiral and irregular galaxies, emitting synchrotron radiation and free-free emission, from Type II and Type Ib supernovae remnants (SNRs) of mass $M \gtrsim 8M_{\odot}$ and HII regions, respectively (Condon, 1992). The characteristics of SFGs radio spectra includes a steep curve of spectral index $\alpha \sim 0.8$ due to synchrotron radiation, and then becomes flat ($\alpha \sim 0.1$) due to free-free emission which predominates at frequencies $\nu \gtrsim 30$ GHz (Condon, 1992), the definition of a synchrotron radiation spectra is shown in Equation 1.4. SFGs are dominating at high redshifts, in other words, there is more star formation (SF) at high redshifts compared to in the local Universe (Padovani, 2016), an illustration of this is shown in Figure 1.6. SF is a process where molecular gas clouds convert into stars under the influence of self-gravity, where the clouds are mainly made up of hydrogen and carbon monoxide. The SF activity occurs in two modes, (i) the starburst mode, where SF is triggered by mergers or dense SF regions, and (ii) star formation rate (SFR) and the stellar mass tight correlation mode (Padovani, 2016). This correlation is called

the main sequence (MS) of SFGs and is described by power-law SFR $\propto M_{\star}^{\alpha}$, stating that the SFR scales with stellar mass $M_{\star}$ for star-forming galaxies, with $\alpha \sim 0.6$ - 1.2 (Popesso et al., 2019). For a given volume in the Universe, SFGs outnumber AGNs, but the rare AGNs are more luminous, about half of the observed radio emissions come from AGNs (Condon and Ransom, 2016).

FR 0 RGs are a newly proposed class of radio galaxies (Padovani, 2016). They are relatively rare, and the main purpose of this thesis is to introduce AGNs and SFGs, which dominate the better-understood radio source counts.

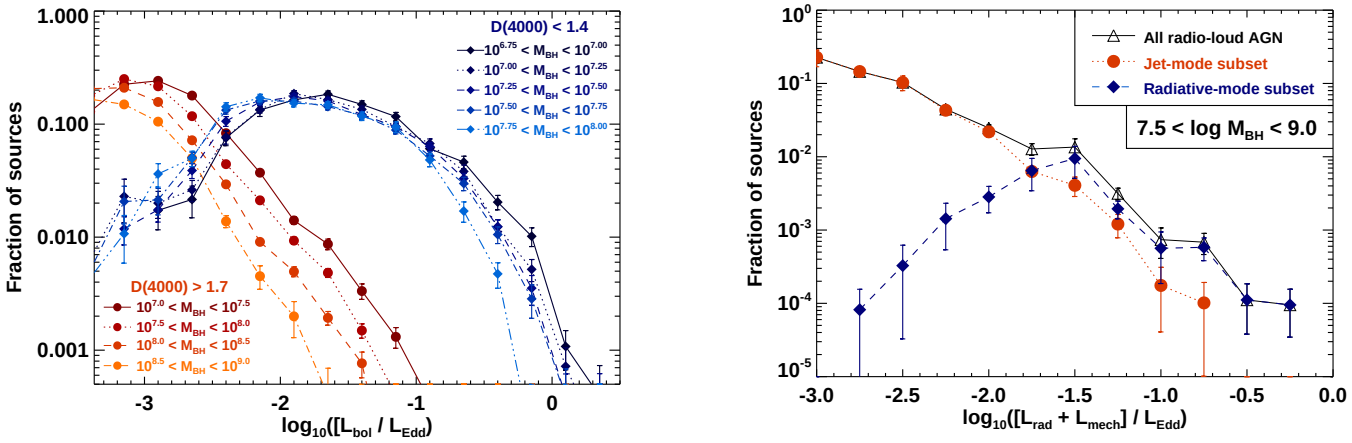

FIGURE 1.5: **Left panel**: the distribution of Eddington ratios of emission line selected AGNs, obtained from the Sloan Digital Sky Survey (SDSS), where the main galaxy sample is split by star-formation activity. D(4000)<1.4 indicate distributions for active star-forming host galaxies, while D(4000)>1.7 are for passive host galaxies, each of the distributions is for a range of masses as shown in the legends. The fractions are plotted within each 0.25 index wide bin in the Eddington ratio. **Right panel**: the distribution of Eddington ratios of radio-loud AGN using the SDSS main galaxy sample, of Eddington limit 10^{-3}, the sample is split into the jet-mode and radiative-mode sources, and again, the fractions are also plotted within 0.25 index. The jet-mode AGN dominates at low Eddington ratios and follows a Power-law distribution with a slope of bout -1.5. The radiative-mode Eddington ratios peaked at a few percentages. The distributions of these two classes show similar characteristics as populations for emission-line AGN in the right panel. Images are directly reproduced from Heckman and Best (2014).

Astronomers often study sources by counting them as a function of flux density, and in most cases, the counts are calculated using the differential source count approach (i.e., the number of sources per flux density per steradians). The count helps understand source population evolution properties as well as Cosmological properties (Padovani, 2016). An example being Figure 1.7 on the left panel, where Padovani (2016) illustrates Euclidean-normalised source counts at 1.4 GHz frequency for three different luminosity evolution models, up to redshift $z = 2$. The number counts were calculated in the case of a pure luminosity evolution defined by $P(z) = P_0(1+z)^k$, where k is the evolution constant (i.e., $k < 0$: negative evolution, $k > 0$: positive evolution, and $k = 0$: no evolution). The left panel of Figure 1.7 shows that when

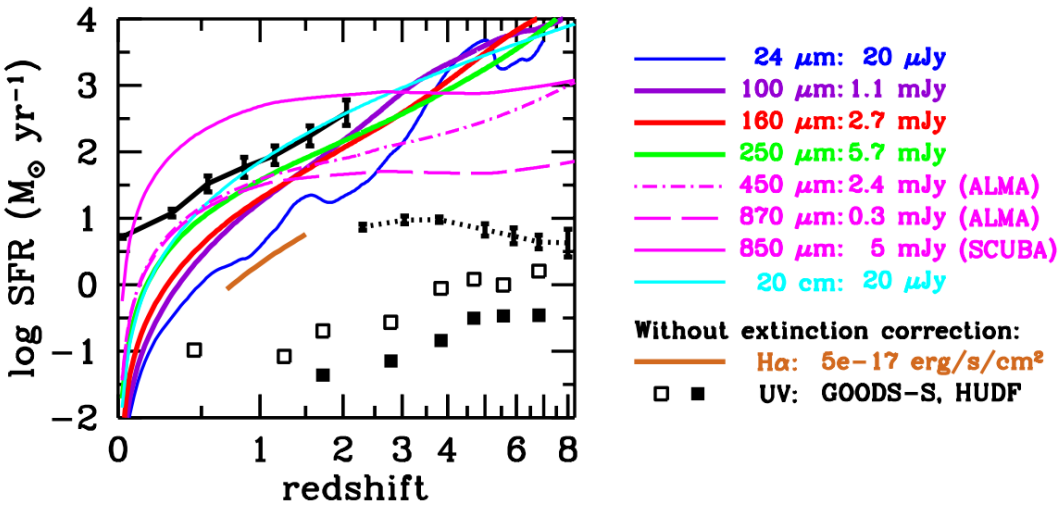

FIGURE 1.6: SFR versus redshift for deep survey data at various wavelengths. The top right legend-like indicate the wavelengths and their corresponding flux limits. The plots (colour coded with wavelength and flux limit) shows that SFR increases with redshift. Image is directly reproduced from Madau and Dickinson (2014).

the cosmological model and spectral index are fixed, source counts depend on the evolution of the source population(s).

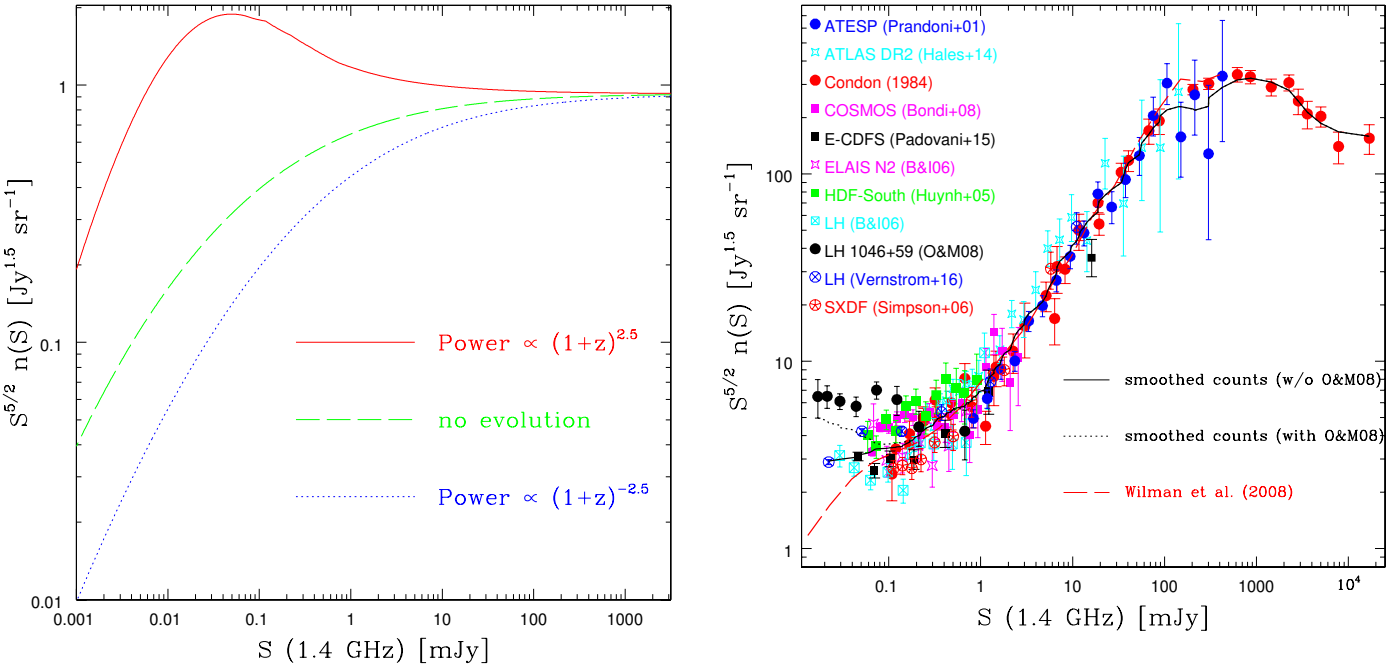

FIGURE 1.7: The Euclidean normalised radio source counts at 1.4 GHz derived from different luminosity evolutions (**left panel**) and various surveys (**right panel**), as indicated in the legends. The solid and dotted black lines represent a smoothed version of the source counts while the red dashed line represent simulated source counts. Images are directly reproduced from Padovani (2016).

The right panel of Figure 1.7 shows a Euclidean-normalised source counts of observed data from various surveys at 1.4 GHz. It shows the source counts undergoing a positive evolution at high flux densities, in other words at high flux densities the source counts are dominated by RL AGNs, and source counts decline down to 1 mJy following a power law, where RQ AGNs and SFGs tend to be residing. At lower flux densities (S $\sim$ 1 mJy) we can see that it is crowded. If we go deep in observations we experience what is known as source confusion for arcsec-scale interferometers (i.e., many sources merge in a single beam), the source counts are scattered. It is believed to be due to cosmic variance and/or inconsistencies in the way authors measure the number of sources. Source confusion will be discussed further in Section 2.6, as it is of key importance in continuum stacking.

1.2 Radio Astronomy Facilities

Depending on the scientific goal, a radio antenna can be used as a transmitting or receiving device. It converts EM radiation from space to electric current here on earth or vice versa, but for astronomy, radio antennas are normally used as receiving devices. A typical radio antenna consists of a dish (a primary reflector) to collect and focus radiation to the secondary reflector (if present); and feeds as wave-guides for transferring incoming radiation to receivers. The same aspects are common to telescopes operating at different wavelengths such as visible (e.g., Walker, 1987), infrared (e.g., Fanson et al., 1998) and ultraviolet (e.g., Davidsen et al., 1992). However, radio antennas can have a different form when operating at longer wavelengths (e.g. low-frequency antennas such as the Low-Frequency Array Haarlem et al., 2013 versus high frequencies such as the Atacama large millimetre array Wootten, 2003). Most radio antennas have steerable dishes, meaning they can point at any direction in the sky controlled remotely. For a typical single-dish antenna, whether steerable or not, the effective area of the dish is defined as

$$A_{eff} = \frac{P}{S_\nu \Delta\nu}, \tag{1.5}$$

where P is the radiative power from a source of flux density S_ν and bandwidth $\Delta\nu$. The radiation power measured from the source can be obtained by reworking Equation 1.5 as follows

$$P = S_\nu A_{eff} \Delta\nu, \tag{1.6}$$

and the power can be described in terms of temperature T_A (for antenna temperature, the power delivered by the antenna through transmission lines) using the equivalent temperature relation

$$T_{eqv} = \frac{P}{k_B \Delta\nu}, \tag{1.7}$$

where k_B is the Boltzmann's constant (Lancaster, 1989). Note that the radiation power is dependent on the effective area of the dish A_{eff}, meaning larger dishes collect more power and result in faint sources being detected. The measured radiation power from a source is not simple as shown from the Equation 1.7 since the incoming radiation from the source has to compete with unwanted power (i.e. telescope receiver noise, background sky noise, the atmosphere and radio frequency interference) (Bradt, 2004), so it is important to perform careful calibration in an attempt to separate those different components. The total radiation power detected by

the antenna plus the unwanted power can be described in terms of temperature and it is called the system temperature $T_{sys} = T_A + T_N$, where T_N is the unwanted power (noise temperature) which can be described as $T_N = T_{sky} + T_{atmosphere} + T_{CMB} + etc.$ in units of Kelvin. The antenna temperature can be extracted from the system temperature by subtracting the noise temperature, but since $T_{sys} > T_A$, then some uncertainties from the noise temperature may occur on T_A, and the uncertainties can be described using the radiometer sensitivity equation,

$$\sigma(T_A) = \frac{T_{sys}}{\sqrt{\Delta t \Delta \nu}}, \tag{1.8}$$

where Δt observational duration and $\Delta \nu$ is the bandwidth. Therefore the measured radiation power from a source becomes more precise for large bandwidth and longer observations. Bandwidth is fixed by design; thus uncertainties in the sky temperature can be reduced by observing at much longer durations (Lancaster, 1989). Generally in astronomy, a space source is considered to be detected when the antenna temperature is at least five times the antenna uncertainties ($5\sigma(T_A)$).

A radio antenna's system performance of whether it is capable of detecting radiation of a particular source during observations can be described through the *system equivalent density* (SEFD), where the SEFD is the flux density of a point source that doubles the T_{sys} when in beam, it accounts for the combined sensitivity of the antenna dish and the receiving system and is given by

$$SEFD = \frac{2k_B T_{sys}}{A_{eff}}. \tag{1.9}$$

The SEFD is measured in units of Jansky, and it also provides the sensitivity measure for calculating the minimum detectable flux density

$$S_{min} = \frac{SEFD}{\sqrt{\Delta t \Delta \nu}} \tag{1.10}$$

The SEFD can be said as the measure of a telescope's sensitivity, where lower SEFD means the telescope is more sensitive. For example, the Very Large Array's 25-metre antennas have SEFD of 250 Jy at X-band while MeerKAT has a combined SEFD at $\sim$ 400 Jy at L-band.

Radio observations can be conducted in two different ways, either through a single-dish antenna or an interferometer where multiple single-dish antennas are linked up forming an array and work simultaneously to portray one large single-dish telescope. However, a single-dish is the simplest way of collecting radiation from a source.

1.2.1 Single Dish

A single dish is a radio antenna whose resolution is defined by $\theta = \frac{\lambda}{D}$, where θ is the angular resolution (the ability to distinguish between two adjacent sources separated by a minimum angular distance), λ is the observed wavelength and D being the diameter of the dish. For example, the HartRAO 26 metre radio antenna operating at 13-centimetre wavelength has an angular resolution $\theta \sim 20$ arcminutes (Jonas, Baart, and Nicolson, 1998). Normally single-dish antennas have small diameters to make movements easy, but the small diameter results in a smaller field of view, a

low angular resolution, lower sensitivity and poor pointing accuracy (Condon and Ransom, 2016). The angular resolution can be improved by increasing the diameter of the dish or by observing at shorter wavelengths. Nowadays single dishes are primarily used for

i. Pulsar searching or observing them since pulsars are easy to separate from confusion and require low-resolution power to observe them;

ii. Complementing interferometers for observing large scale structures and serving as part of interferometers (e.g., Heywood et al., 2019);

iii. Spectroscopic observations of low brightness sources that cannot be confused, for example, the searching for extraterrestrial signals, with projects like the SETI, the search for extraterrestrial intelligence (Wright, 2002).

1.2.2 Interferometery

Two Element Interferometry

As with cameras, the angular resolution of a single dish is diffraction-limited, and it pushed scientists and engineers to find better techniques which led to interferometry and aperture synthesis (Ryle and Hewish, 1960). The angular resolution achievable by an interferometer is defined as $\theta = 1.22\frac{\lambda}{B_{max}}$, where B_{max} is the maximum distance between a pair of antennas (called the maximum baseline) of the interferometer. The short baselines between closely located antennas, as shown in Figure 1.10 give information about large scale structures. In contrast, the longer baselines give information about small scale structures. While an interferometer's angular resolution at a given wavelength depends on the array configuration and observing wavelength, the sensitivity of the interferometer depends mainly on the receiver electronics characteristics and collecting area of each element forming the array (Boccardi et al., 2017), and is captured by the SEFD as mentioned earlier. A very sensitive interferometer used in this thesis is discussed in Section 1.2.2.

Figure 1.8 shows a schematic diagram of a two element interferometer, where EM radiation from a distant source is collected by the two single dishes separated by distance B known as the baseline, but the signal will not reach both the dishes at the same time due to the separation distance B between the dishes and non-zenith observing direction. The radiation signals measured from the two dishes undergoes what is known as correlation, which happens within the correlator, where the signals are multiplied and averaged in time, and frequency intervals. The resultant response signal measured by the interferometer is a complex (noise corrupted) function known as *visibility* and is described by the van Cittert- Zernike theorem (Thompson, 1999)

$$V_{ij}(u,v,w) = W(u,v,w)\int_l\int_m \frac{A(l,m)I_\lambda(l,m)}{\sqrt{1-l^2-m^2}} e^{-i2\pi\left(ul+vm+w(\sqrt{1-l^2-m^2}-1)\right)} dldm, \tag{1.11}$$

where $W(u,v,w)$ is the sampling function, also known as the point spread function (PSF) and is defined by the configuration of the interferometer, $I_\lambda(l,m)$ is the sky brightness distribution function, $A(l,m)$ is the primary beam function in cosine coordinates (l,m), and (u,v,w) being the projected baseline coordinates measured in wavelength, with u pointing parallel to the east-west and v to the north-south, and w pointing in the centre of the image plane (i.e., the phase centre), an illustration

diagram is shown in Figure 1.9. Therefore, the *uv*-plane or *uv*-coverage gives information about the visibility measurements at a certain point. The *uv*-plane is always incomplete for every interferometer, it can be filled by adding more antennas and increasing the observational duration for more than 12 hours for example, in that case, the rotation of the Earth will cause the baselines to rotate in time and help fill in the absent information (i.e., a single baseline will sample a full track or an eclipse in the *uv*-plane) (Boccardi et al., 2017). However, the centre area of the uv-plane corresponding to distances less than the smallest baselines will always remain not sampled to some extend. This cause some emissions not to be recorded by the interferometer. From the visibility function, we are interested in the sky brightness distribution function, the two functions are related through Fourier transform,

$$I_\lambda(l,m) = \mathscr{F}^{-1}\{V(u,v,w)\}, \quad V(u,v,w) = \mathscr{F}\{I_\lambda(l,m)\} \tag{1.12}$$

meaning a sky brightness distribution can be reconstructed by calculating the inverse Fourier transform ($\mathscr{F}^{-1}$) of the interferometer's visibility function, and also corresponding the visibilities can be obtained by Fourier transforming ($\mathscr{F}$) the sky brightness distribution (Offringa and Smirnov, 2017), but an interferometer samples incomplete Fourier transformed sky brightness distribution function $I_\lambda(l,m)$, information is missing, and the sky brightness distribution cannot be completely measured. Instead, it can be estimated or reconstructed by convolving the visibilities with the interferometer's PSF $W(u,v,w)$ and applying deconvolution to get accurate flux density measurements of the sky. Deconvolution models that are typically used are based on the Högbom CLEAN (Hogbom and Brouw, 1974) and its variants (Wakker and Schwarz, 1988; Cornwell, 2008; Rau and Cornwell, 2011; Smirnov, 2011).

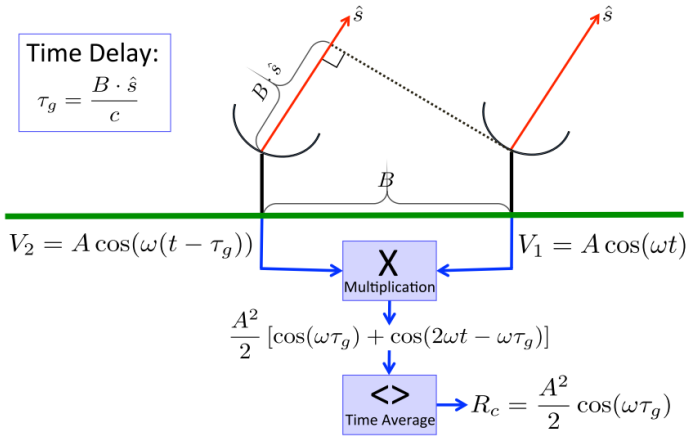

FIGURE 1.8: An illustration of a two-element interferometer. The radiation emitted by distant sources arrives at the two dishes separated by a baseline distance B in the form of a plane wave in direction $\hat{s}$. The radiation signal measured by two antennas are the same, assuming the same pointing direction, but antenna on the left experiences a geometric time delay of $\tau_{\hat{s}}$. Both radiation signals from two antennas are then multiplied and averaged by the correlator, and result in a signal response R_c. Image directly reproduced from Bouman et al. (2016).

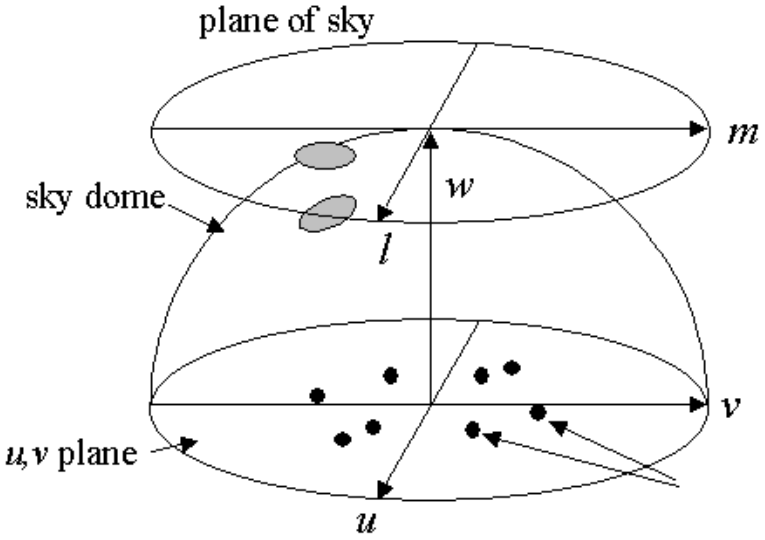

FIGURE 1.9: (uvw) projected baseline coordinates illustration diagram. The sky dome and its approximation as a flat "plane of the sky" are shown. Image is directly reproduced from NJIT radio astronomy course notes.

The visibility function (Equation 1.11) can also be represented in terms of the radio interferometer measurement equation (RIME) (Hamaker, Bregman, and Sault, 1996). The RIME describes robustly and compactly all the effects that may occur during interferometric measurements, for more discussion about the RIME see Smirnov (2011). The simpler case of the visibility function described in terms of the RIME

$$\tilde{V}_{ij} = J_{ij}V_{ij} + \epsilon_{ij} + \eta_{ij}, \tag{1.13}$$

where $\tilde{V}_{ij}$ represents the observed visibilities, J_{ij} is the corruption noise in baselines between telescopes i and j , V_{ij} are the true visibilities, ϵ_{ij} is the correlator noise and η_{ij} represents additional noise.

The MeerKAT Telescope

The Meer Karoo Array Telescope (MeerKAT) is a next-generation interferometer located in the Karoo region of the Northern Cape province in South Africa, the geographical coordinates of the telescope are of longitude 21° 26′ east and latitude 30° 42′ south. The telescope is a precursor to the Square Kilometre Array (SKA) mid-frequency array and consists of 64 offset Gregorian design antennas each of diameter 13.5 metres. The offset Gregorian design ensures that there is no blockage of the incoming radiation during observations. The advantages of the unblocked aperture are (i) to provide high aperture efficiency for improved sensitivity, (ii) for reducing the system temperature by limiting the pickup from ground radiation, and (iii) lowering the sensitivity of the Radio Frequency Interference (RFI) and primary beam sidelobes (Mauch et al., 2019). All of these enables high dynamic range observations which are critical to the stacking experiments explored in this thesis, a point that is returned to later. Figure 1.10 shows that the majority of the antennas are located around a diameter of approximately 1 kilometre from the centre core enabling high surface brightness sensitivity, and the maximum baseline between the antennas is 8 kilometres.

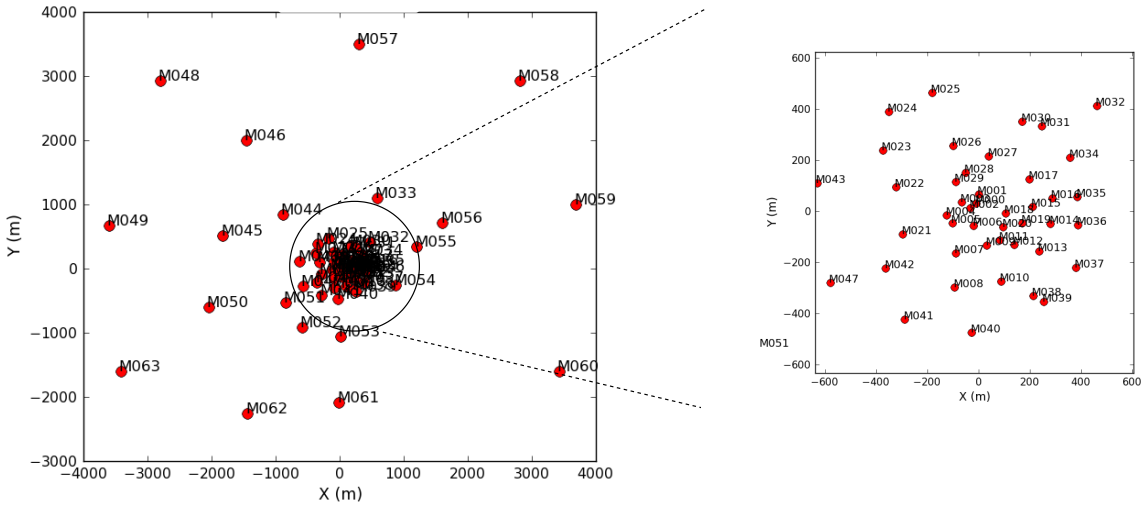

FIGURE 1.10: Antenna positions for the MeerKAT telescope. The baseline lengths range from 20 m to 8 km, with a majority of antennas are concentrated at the centre core region (i.e., the right panel is a zoomed-in section of the antennas at the centre core region and how they are distributed inside the 1 km core). The antennas are named "m000" to "m063".

Each antenna consists of three main components, namely the antenna positioner, receivers and digitisers. The antenna positioner is made up of a 13.5 metres main reflector and 3.8 metres sub-reflector, and the entire framework is mounted on top of the pedestal. A schematic diagram of a MeerKAT single dish structure is illustrated in Figure 1.11. The mount is an azimuth and elevation type, making the antenna dish to be steerable at azimuth range -185° to +275° and elevation range 15° to 88°. During observations, EM radiation is reflected from the main reflector to the sub-reflector and then ends up on the receiver indexer mounting the receivers and digitisers. The receivers are for measuring EM radiation and converts it into voltage. Three receivers currently installed measure EM radiation at different frequency bands: L-band (900 - 1670 MHz), S-band (1750 - 3500 MHz) and UHF-band (580 - 1015 MHz). These receivers are rotated by the indexer for a desired observational frequency. For each receiver, there is a digitiser for converting the measured EM radiation into a voltage signal. Observations for this thesis were done using the S-band, which is discussed in Section 3.1.2. Digitisers convert voltage signal from a receiver into a digital signal which is transported to the processing building where it undergoes various processing stages,with cross-correlation (multiplying and averaging signals to form visibilities) being one of them. The visibilities are recorded and transported through fibre optics to the Centre of High-Performance Computing (CHPC) in Cape Town, where they are stored for imaging and analysis.

MeerKAT's angular resolution is $\sim$ 8 arcsec at L-band and $\sim$ 4 arcsec at S-band (which depends strongly on the chosen imaging weights). The instrument is the most sensitive radio interferometer in the Southern Hemisphere for capturing deep and high fidelity centimetre wavelength emission and detecting macro-Jansky radio sources (Booth and Jonas, 2009). The telescope is also capable of sensitive observations of transient sources. The SEFD of the array is $\sim$ 400 Jy at L-band combined with a large field of view (FoV), results in a large survey speed. The extension of

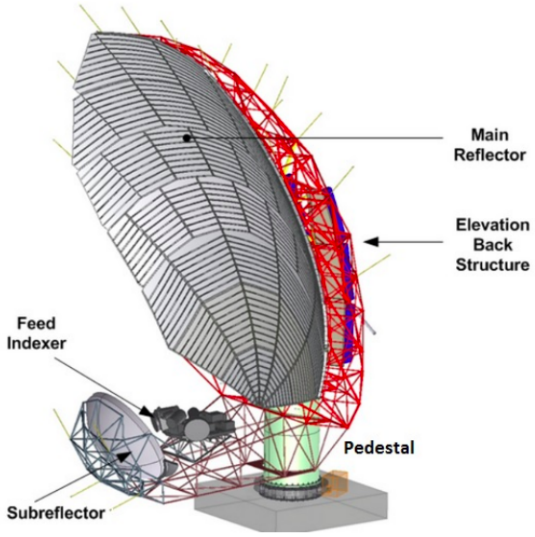

FIGURE 1.11: MeerKAT single-dish schematic diagram structure. The dish is of 13.5 metres in diameter, where incoming light gets reflected from the main reflector dish to a sub-reflector of 3.8 metres then to the detectors suspended above the main reflector. Image is directly reproduced from Jonas (2016).

MeerKAT by additional 20 dishes and maximum baseline of up to 16 km will increase the array's sensitivity by up to 50% and the angular resolution by a factor of ~ 2.

Time And Bandwidth Smearing

We now know a radio interferometer measures samples of the Fourier transform of the sky brightness distribution. In order to reconstruct high-fidelity, wide-field images of the sky brightness distribution, these visibilities must be recorded at sufficiently high time and frequency resolution; otherwise, the images will suffer from *time and bandwidth smearing*. Smearing is unavoidable and occurs inside the correlator during the averaging when sampling the visibilities in frequency and time intervals. The smearing mainly decreases the flux density amplitude of the sources that are located far from the phase centre within the FoV. Furthermore, this effect increases with baseline length (Atemkeng et al., 2016). The FoV of an interferometer is defined as $\theta_{FoV} = \frac{\lambda}{D}$, where λ is the observed wavelength, and D is the diameter of a single dish antenna of an interferometer (assuming a heterogeneous array). Smearing not only decreases the flux density but also distorts the PSF (particularly far away from the phase centre) since different baselines sample different Fourier modes.

Figure 1.12 shows the effect of smearing on a 1 Jy source, observed with the Very Large Array (VLA) C configuration at 1.4 GHz frequency, by plotting the source's apparent flux density as a function of the distance from the phase centre. The figure shows that to avoid smearing, the averaging should be kept at $\sim$ 10 s and $\sim$ 125 kHz. In the case of aggressive averaging, say at $\sim$ 50 s and $\sim$ 5 MHz the recovered flux density will decrease rapidly towards the edge from the phase centre. For this thesis, smearing is an important aspect to avoid the decrease in flux density amplitude for our stacking results, and therefore precautions are taken when choosing the averaging intervals.

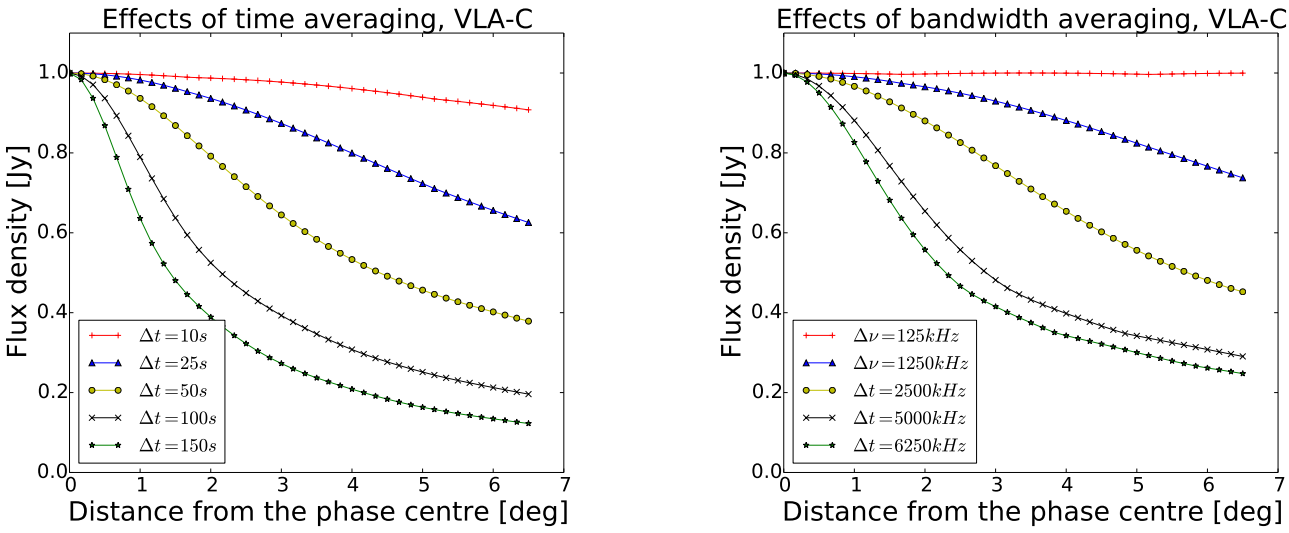

FIGURE 1.12: Effects of time and frequency averaging on the visibility function, shown on a plot of flux density as a function the distance from the phase centre for a 1 Jy source, observed with the VLA-C at 1.4 GHz frequency. (**Left panel**) frequency interval is fixed at 125 kHz, and the time interval varies from 10 to 150 s. (**Right panel**) time interval fixed at 1 s, frequency interval varies from 125 to 6250 kHz. Figures are directly reproduced from Atemkeng et al. (2016).

1.3 Thesis objectives and outline

The key objective of this project is to perform a suite of visibility stacking experiments on realistic synthetic data generated from the TRECS SKA simulations (Bonaldi and Team, 2018). This allows us to test how this approach compares with the traditional image-plane stacking approach. Parameters to vary will be the CLEAN depth, stacking depth and the maximum distance from the phase centre. We can anticipate that confusion will limit stacking with MeerKAT, due to the μJy-level sensitivity and $\sim$10 arcsec angular resolution of the telescope. Most of the galaxies are marginally or completely undetected with a typical MeerKAT observation, but their median flux can in principle be recovered with the stacking approach.

This thesis is organised as follows: Chapter 2 outlines the process and scientific application of image-plane and visibility stacking. Chapter 3 describes the simulated interferometric observations framework developed and the stacking experiments to be performed. Chapter 4 presents the simulated and real MeerKAT data results, and conclusions are drawn in Chapter 5.

Chapter 2

Stacking

2.1 Introduction

For every wavelength observation in astronomy, there is always a need to extract information that lies below the noise threshold and thus can be potentially extracted using *stacking*. Stacking is a technique to combine image or visibility data from multiple sources that are below the noise level (i.e. individually undetectable) to increase the signal-to-noise ratio (SNR) for that particular sample and make a statistical detection. However, it requires the 2D (or 3D) positions of the catalogue of sources to be known a priori from previous observations of a different frequency where the sources are more easily detectable (see, e.g., Garn and Alexander, 2009).

The stacking technique has proven to be powerful for studying radio emission from the faint radio source population (see, Section 2.4). It will be important to carry out statistical studies of some of the MeerKAT image-plane Large Survey Projects. However, MeerKAT's confusion limit of ~ 1 μJy/beam at L-band will pose a significant challenge to the full utilisation of this technique and create biases that are yet to be characterised and understood, which this thesis aims to begin. There are two methods of stacking, namely image and visibility stacking, each with their pros and cons which will be discussed in Section 2.2 and 2.3.

2.2 Image stacking

Image stacking, as the name suggests, is defined as stacking sources on the image plane. In the literature, there are many ways of performing image stacking, but two primary examples are (i) stacking on a pixel-by-pixel basis (see, e.g., White et al., 2006), or (ii) modelling histograms of flux density distributions (see, e.g., Mitchell-Wynne et al., 2014). In this thesis, image stacking on a pixel-by-pixel basis will be employed.

Image stacking on a pixel-by-pixel basis is performed by generating a full-image map, which may be an interferometric map generated via self-calibration and deconvolution. This map is then used to make small cut-out images centred on each target source position included in the stacked sample. The target source position where stacking is performed can be defined as *stacking positions* while the cut-out images can be referred to as *postage stamps*. The postage stamps are combined all together using either the traditional mean, weighted mean or the median. A mean combination is defined as

$$\overline{x} = \frac{\Sigma x}{n}, \tag{2.1}$$

where $\overline{x}$ the mean flux density at each pixel location to produce a mean stacked image, Σx is the sum of flux densities at each pixel location and n is the number of stacked pixels per stacking position. If the noise is non-uniform across the image, a noise image is necessary. The weighted mean can be used to account for differing local noise by weighting the contribution of each source, and weighted mean stacking is defined as

$$\overline{x}_{w_i} = \frac{\Sigma_i^n (x_i \times w_i)}{\Sigma_{i=1}^n w_i}, \tag{2.2}$$

where $\Sigma_i^n (x_i \times w_i)$ is the sum of flux densities at each pixel location and the weight contribution of each stacking position, $\Sigma_{i=1}^n w_i$ is the sum of the contributing weights. The weights are defined as $w_i = 1/\sigma_i^2$, where σ_i is an estimate of the noise contributed by a source at stacking position i. As discussed by White et al. (2006), median stacking is less sensitive to outliers compared to mean stacking methods. Figure 2.1 shows a comparison in results that occurs when using a traditional mean or median stacking, the mean stacked images are noticeably noisier than the median, with nearby bright sources having more effect on the stacking results. The noise level on the mean images is $\sim$ 3 to 5 times than the median. These radio stacked images are of 1.4 GHz for the faintest flux density bins, and all have a size of 41 x 41 pixel^2, with a corresponding flux density range of sources used to create the stacked image given below each sub-image.

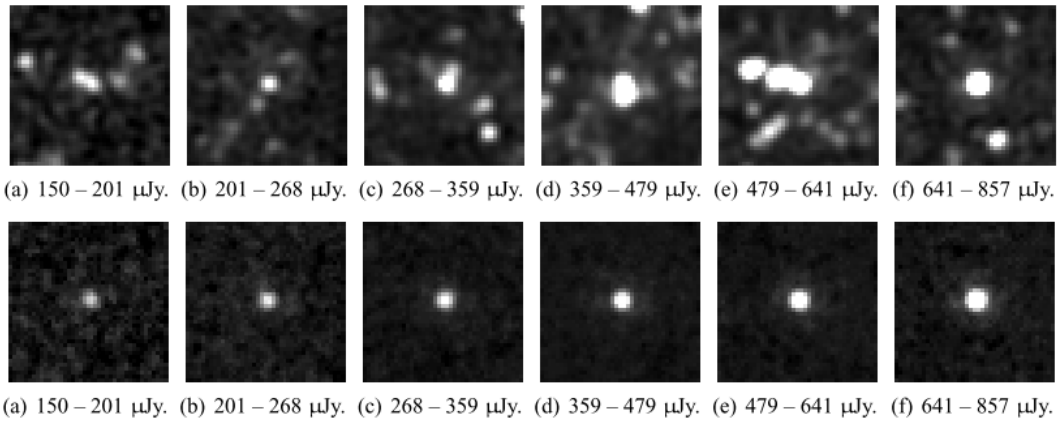

FIGURE 2.1: Comparison in results from mean (**top panel**) and median (**bottom panel**) stacking, all the images are of 1.4 GHz frequency having size of 41 x 41 pixel^2 The corresponding flux density range of sources used to create the stacked image given below each sub-image. Figures are directly reproduced from Garn and Alexander (2008).

The image stacking method, when used to stack interferometric data, may result in (i) CLEAN artefacts and (ii) correlated noise structure in the image plane, on the resultant stacked image. This is due to interferometric observations not being a direct imaging method like an optical camera, for example. For interferometric observations, the final image is obtained by self-calibration and deconvolution, which may later pose problems to the stacking due to the correlated noise in the image-domain. Figure 2.2 shows a simple image stacking on a pixel x pixel basis illustration. A list of faint sources is obtained from a catalogue of different wavelength where their emissions were detectable. For each stacking position, a postage stamp of size $\sim$ 64 x 64 pixel^2 is extracted from the full image, then all postage stamps are combined on a pixel x pixel basis and result in a stacked image of higher SNR than each postage stamps.

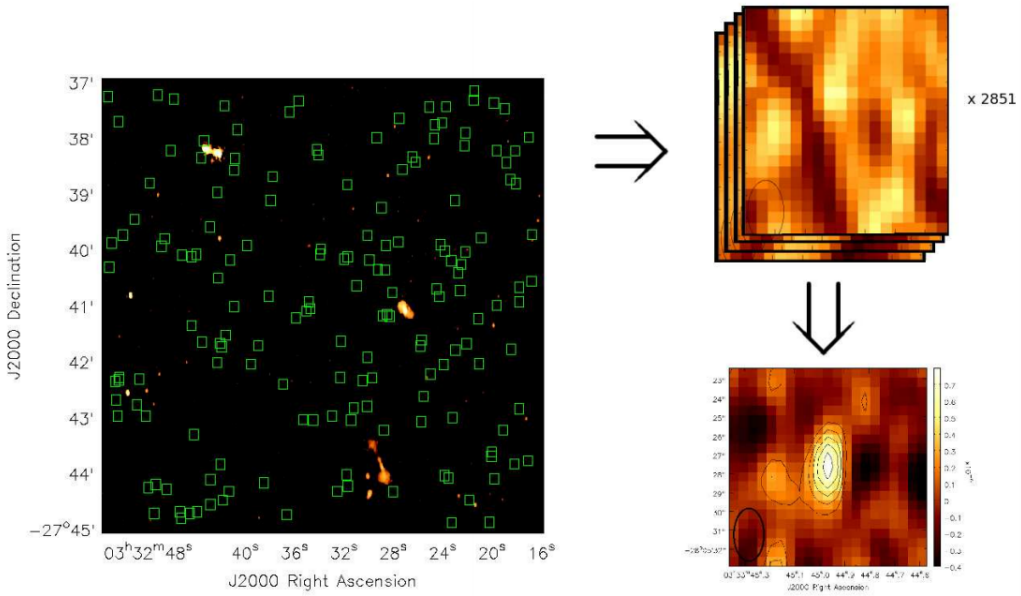

FIGURE 2.2: An image stacking example. **Left panel**: an image from the Extended Chandra deep field-south (ECDFS) observation, each green square indicates a position of an individual faint source. **Top right panel**: postage stamps being stacked all together and that results in a stacked image shown on the **bottom right panel** of higher SNR than individual postage stamps. Reproduced directly from Lindroos (2014).

2.3 Visibility stacking

Stacking on the visibility plane (*uv*-plane) is a better approach to avoid artefacts that come with the image stacking method, and such method of stacking is called visibility stacking also known as *uv*-stacking. Visibility stacking combines visibilities of target sources before the image is created. It works by first creating a copy of the full visibility data for each target source and then phase rotate (changing the phase centre) to each stacking position. It then combines the visibilities for each target source using similar combinations as image stacking (i.e. mean, weighted mean or a median combination) to produce a stacked visibility data of target sources, of lower noise with the same *uv*-coverage as the original data set, and the stacked source located at the phase centre. The new visibility stacked data set can either be imaged using interferometric imaging techniques discussed in Section 1.2.2 or modelled directly in the *uv* domain to estimate the average flux density and source sizes of the stacked data. The advantages of working on the visibility plane are in particular (i) little to no clean artefacts is experienced due to no imaging required, and (ii) much better size (and therefore better brightness temperature) measurements of the average population. However, it is more computationally expensive, so this project is looking at where the scientific yield is worth the additional processing with MeerKAT. In comparison, the pros and cons of working on the image plane are listed in Table 2.1.

In this thesis, visibility stacking is performed by employing an algorithm developed by Lindroos et al. (2014). The algorithm has been developed to apply to any radio interferometric data set, also to handle effects that come with mosaic and wide-field VLBI observations. Its performance was tested on simulated data mimicking the

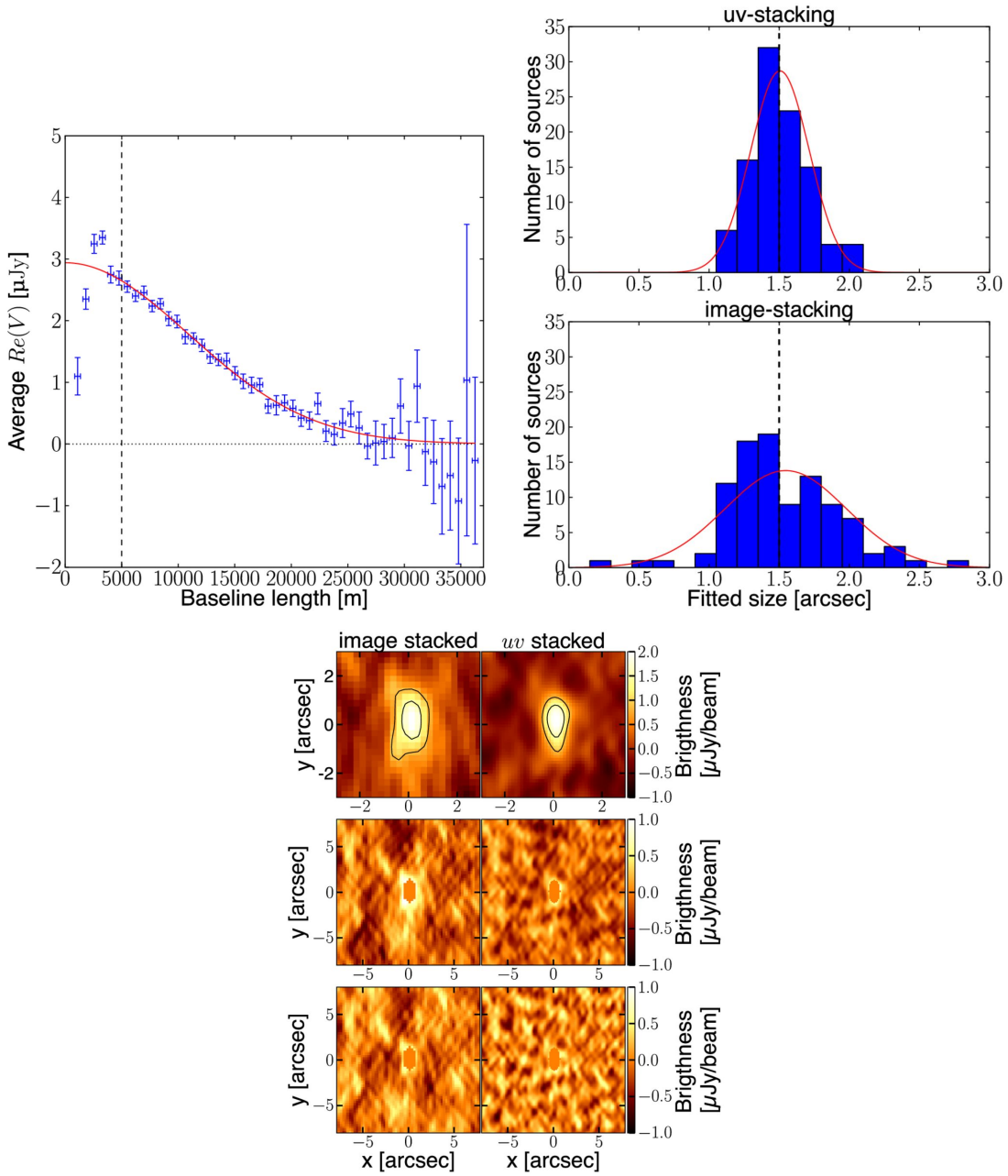

FIGURE 2.3: VLA simulation of extended sources stacking results from Lindroos et al. (2014). **Top left panel**: VLA simulation of extended sources stacking results from Lindroos et al. (2014). **Top left panel**: The average of the real part of the flux density visibility as a function of the baseline, the red curve indicates the average fitted sizes and fluxes using visibilities from baselines greater than 5000 m. Also for short baselines (less than 5000 m) the average flux density does not fit, due to the sources not being fully resolved. **Top right panel**: The distribution of fitted sizes for visibility and image stacking data, the visibility stacking is narrower compared to the image stacking, which indicates a higher precision towards the true fitted size. The dashed line indicates true size. **Bottom panel**: Image and visibility stacked postage stamps, both postage stamps show variations which results from nearby bright sources and variations are more visible on the image stacking (row one). The central pixels are masked out (row two). Short baselines are removed, central pixels are masked out, and visibility stacking is implemented, the same thing is done for image stacking, by converting the image into visibilities through Fourier Transform. The procedure still favours visibility over image stacking, due to more variations still present in the image stacking postage stamp (row three).

Atacama Large Millimetre Array (ALMA) and the Very Large Array (VLA) observations for deep extragalactic surveys and compared to image stacking. From the comparison, visibility stacking was found to yield more robust results than image stacking, the comparison results between image and visibility stacking are shown in Figure 2.3. This is due to having access to the visibility data after the stacking process, were unwanted data and other effects that may affect the stacking negatively can be removed. Therefore this supports visibility stacking being a powerful method for stacking interferometric data. The algorithm uses the following equation to calculate the stacked visibilities for target sources of known positions within a single pointing,

$$V_{stack} = \frac{\Sigma_{i=1}^{N} W_i \frac{1}{A_N(\hat{S}_i)} e^{\frac{2\pi}{\lambda} jB.(\hat{S}_0 - \hat{S}_i)}}{\Sigma_{i=1}^{N} W_i}, \tag{2.3}$$

where W_i is the weight of a target source at stacking position i, $A_N(\hat{S}_i)$ is the primary beam attenuation in the direction of stacking position i, λ is the observing wavelength, B is the visibility baseline, $\hat{S}_0$ is the unit vector pointing to the phase centre and $\hat{S}_i$ is the unit vector pointing to the stacking position i. Using this equation does not duplicate the visibilities, meaning there is no increase in the size of the data set. Another advantage is that the visibilities are computed independently, making it easier for parallelism and faster execution for large data sets.

TABLE 2.1: Comparison between image and visibility stacking

Image stacking	**Visibility stacking**
Sensitive to CLEAN artefacts	Little to No CLEAN artefacts
Less computation power required	Computationally expensive
Does not allow the removal of unwanted data	Allows for the removal of unwanted data post stacking

2.4 Science with stacking

The majority of radio sky surveys are dominated by the faint radio sky population. This has in part driven by improvement in sensitivity of radio telescopes and motivated stacking experiments in the past, to better constrain our knowledge about the radio populations below the noise threshold. Below are examples of stacking experiments in literature for studies of the faint radio sky population.

2.4.1 Continuum stacking

Dunne et al. (2009) stacked the Very Long Array (VLA) and Giant Metre-wave Telescope (GMRT) continuum images observed at 610 and 1400 MHz frequencies, using infra-red positions from the United Kingdom Infrared Telescope (UKIRT) Deep Sky Survey, to investigate the average star formation (SF) histories from various classes of K-selected galaxies with very faint flux densities ($\sim \mu$Jy). Figure 2.4 shows one of the methods used to extract the star formation history, which is the radio derived star formation rate density (SFRD). They aimed to trace whether AGN or SF contribute towards the radio source populations at low flux densities (< 100 μJy) and find that their radio-derived SFRD agrees very well with the literature values at up

to redshift $z \sim 2$, followed by a steeper decline at higher redshifts than other tracers. They suggest the reason is perhaps that radio emission might be failing as an SF rate tracer at higher redshifts, for example, due to unmodelled evolution of the radio-FIR correlation. From the results, they conclude that AGN do not strongly contribute to the averaged radio emission of stacked K-selected galaxies at flux densities 5 - 20 μJy.

Zwart et al. (2014) studied the SF history of high redshift galaxies in the K_s band, star formation rates (SFRs) and specific SFRs (SSFRs), and also tested the SSFRs determined from semi-analytic models. The approach used was via stacking 1.4 GHz VLA images using positions from the Vista Deep Extragalactic Observations (VIDEO) survey. The selected sample was of $K_s < 23.5$, redshift $0 < z < 5$, then split into different types of galaxy populations (elliptical, irregular and starburst) and stacked per population. The median stacked results were used to determine the stacked flux density of each population instead of weighted-mean results because the median is less sensitive to noise outliers. See Figure 2.6 for weighted-mean and median stacked images, and their error maps. The obtained stacked flux density was used to calculate the SFR, then the SSFR. They find that for the full sample their Mass gradient (β) of SSFR are consistent with those from the literature but inconsistent with results from the semi-analytic models. For the starburst sample, the results agree with those from the literature (see Figure 2.5).

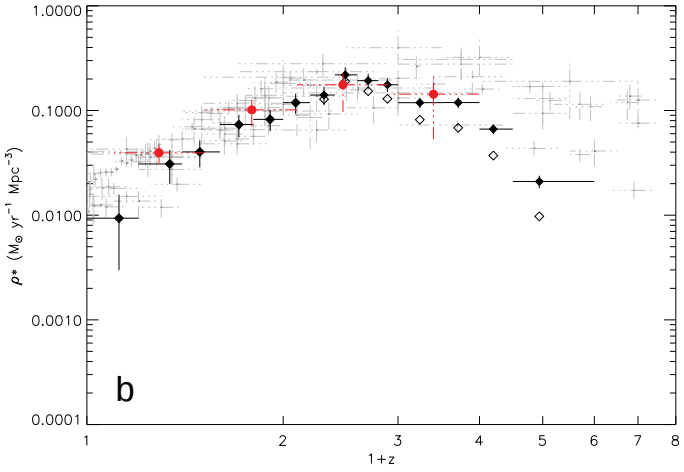

FIGURE 2.4: Radio derived SFRD vs redshift z. The SFRD is derived by converting stacked luminosity at frequency 1400 MHz to the star formation rate (SFR) using the method from Bell (2003). The shaded symbols show SFRD values that are corrected for incompleteness and unshaded are not corrected, both red circles are data obtained from literature and derived from 1400 MHz frequency using methods from Bell (2003). The grey data points are from Hopkins and Beacom (2006), and the radio derived SFRD shows consistency with the data up to $z \sim 2$, but drops when going further. Reproduced directly from Dunne et al. (2009).

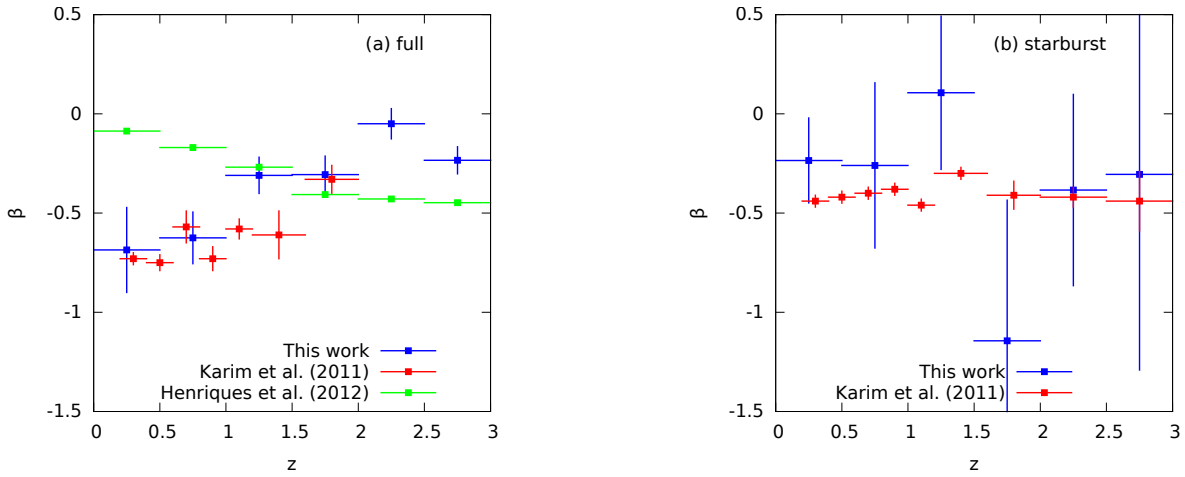

FIGURE 2.5: Mass gradient (β) of SSFR vs. red-shift (z) for full (**left panel**) and star-bust (**right panel**), compared with literature. The green points represent results from the semi-analytic model, red are from literature and blue are from Zwart et al. (2014). Figures are directly reproduced from Zwart et al. (2014).

2.4.2 Spectral line stacking

Spectral line stacking (or 3D stacking) is not entirely different compared to stacking on continuum data (2D stacking). For 3D image stacking, a 3D data cube is generated. An illustration of a 3D data cube is shown in Figure 2.7, the data cube is from the ATLAS^{3D} HI survey (Serra et al., 2012), and it shows a bright galaxy in the central region. The cube is in coordinates of RA, DEC and velocity v. Stacking is performed on a cube, for each of the N undetected target sources of known positions (from other wavelengths). Firstly, each source is centred at zero velocity by shifting its spectrum to rest frequency, then stacking is performed, and the result is a stacked data cube.

Bera et al. (2019) measured the average HI mass of 447 blue star-forming galaxies of absolute magnitude in B filter (M_B) $\leq$ -17 and redshift 0.2 < z < 0.4, by stacking their shifted spectra, observed with the upgraded Giant Metrewave Radio Telescope (uGMRT) using positions from EGS, DEEP2 and DEEP3 surveys. The spectrum in Figure 2.8 shows a HI detection with integration Luminosity of L_{HI} = (2.10 $\pm$ 0.30)$\times$ 10^4 Jy Mpc^2 km^{-1} and this luminosity was used to calculate the average HI mass using the formula for an optically thin HI emission:

$$M_{HI} = 2.343 \times 10^5 \int L_{HI} dv, \tag{2.4}$$

where M_{HI} is the HI mass, L_{HI} is the HI luminosity with respect to velocity resolution v. Applying this formula the average HI mass was found to be $< M_{HI} >$ = (4.93 $\pm$ 0.70) $\times$ 10^9 $M_\odot$ which is found to agree with the values for star-forming galaxies in the local Universe.

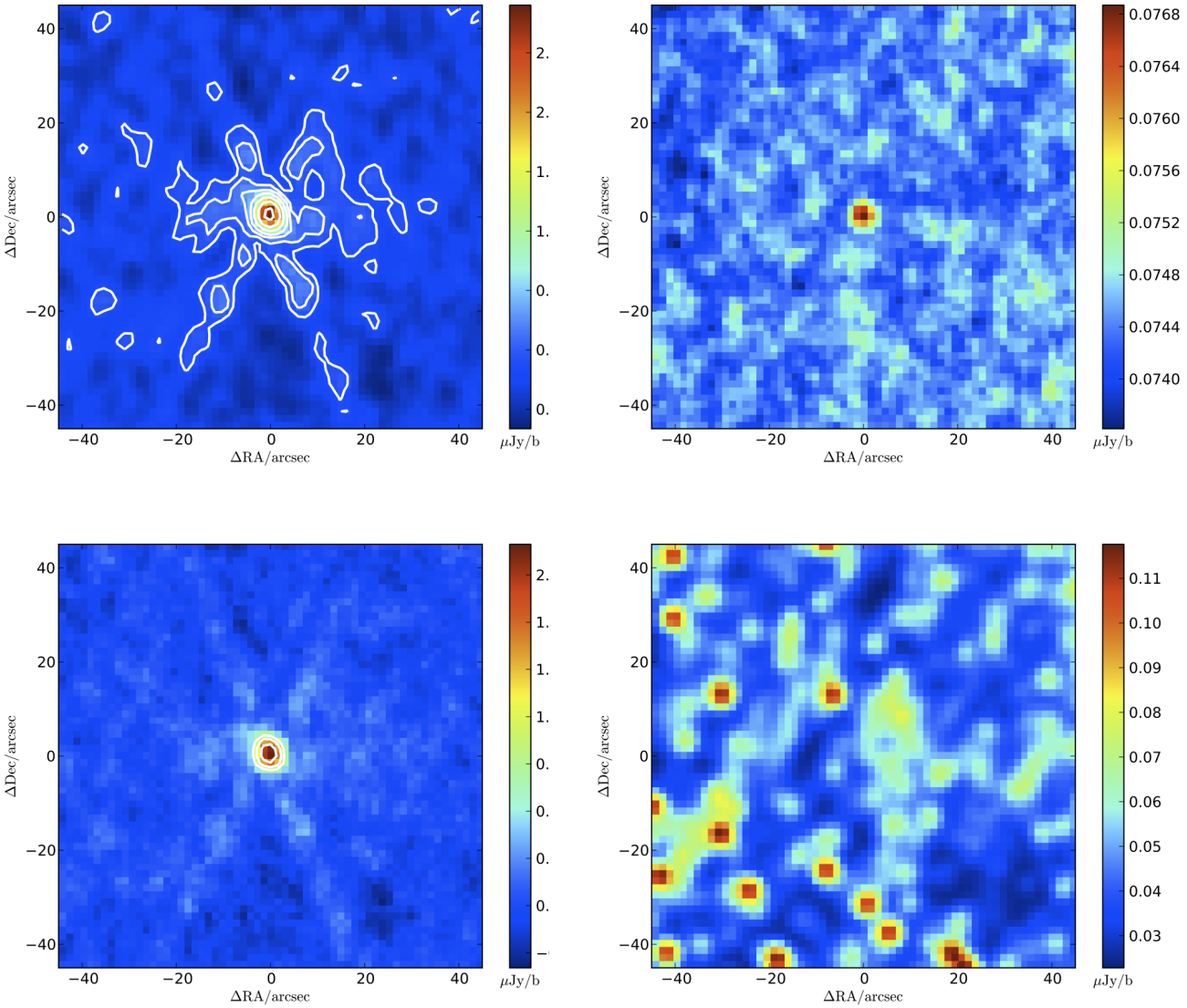

FIGURE 2.6: 1.4 GHz stacked images and their standard-error maps. Each image is a postage stamp of size 41 × 41-pixel, with a scale of 1.5 arcsec/pixel. **Top left panel**: is the weight mean stacked image and its error map (**top right panel**) showing that there is more noise at the central pixel, and might affect the stacking results. **Bottom left panel**: the median stacked image and its error map (**bottom right panel**) where the noise structure is consistent with Gaussian noise. Figures are directly reproduced from Zwart et al. (2014).

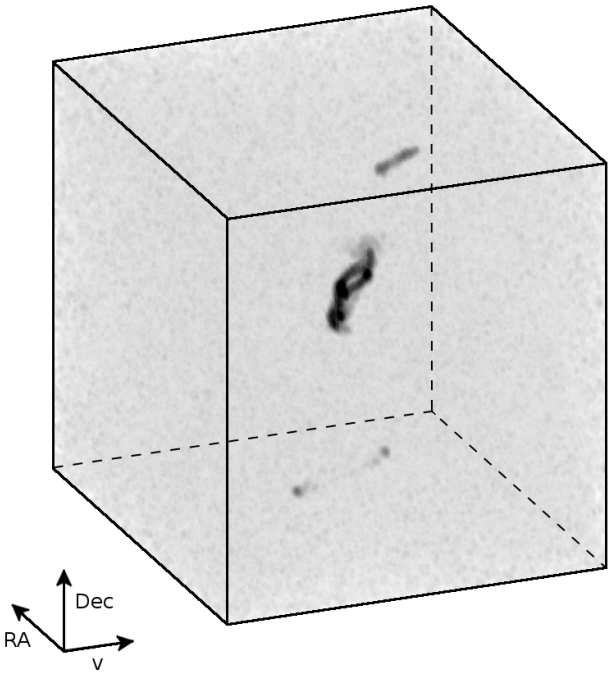

FIGURE 2.7: An illustration of a 3D data cube. Figure are directly reproduced from Serra et al. (2015).

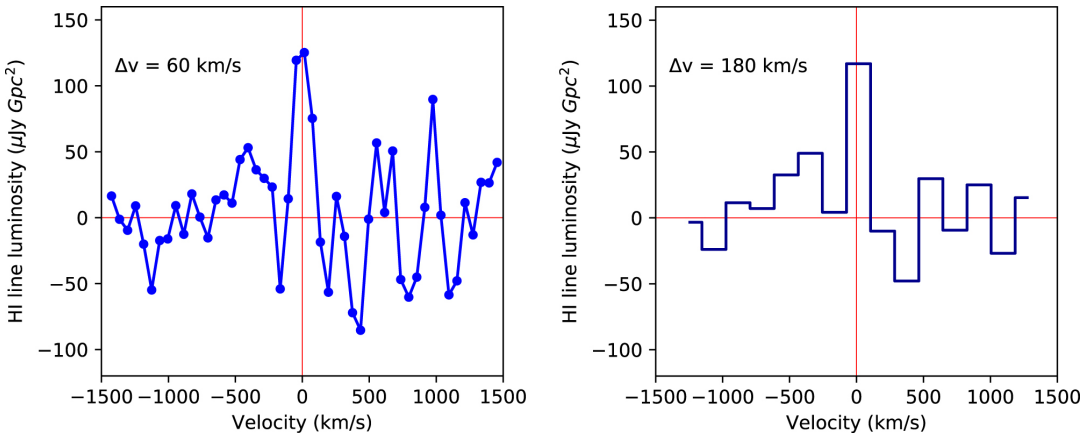

FIGURE 2.8: HI line (21 cm) emission stacked spectrum of 445 blue star-forming galaxies observed with the uGMRT at velocity resolutions 60 kms^{-1} (**left panel**) and 180 kms^{-1} (**right panel**). Figures are directly reproduced from Bera et al. (2019).

2.5 Enhanced calibration with visibility stacking

Any interferometric dataset requires what is known as calibration. Calibration is an interferometric method for estimating and correcting for instrumental, ionospheric, and tropospheric errors, amongst others, in the observed visibilities. A typical interferometric observation will have a calibrator field, which is a field of simple, well modelled source structure and perhaps also well constrained integrated flux density. The calibrator field observations can be used to interpolate complex gain corrections onto the target field, in what is known as cross-calibration (e.g. Grobler et al., 2014a). This standard way of calibration can be refined further through a process known as self-calibration (Grobler et al., 2014b). In self-calibration, the observed sources with sufficient SNR are used as a model to calibrating the complex gains towards the target field. In VLBI observations, this process is often not applicable due to the low sky density and generally lower flux density of high-brightness temperature emission ($\gtrsim 10^6$ K). More generally, this process is often not applicable to faint sources observed within a wide field of view, and that is where visibility stacking may be particularly useful to enhance calibration on a statistical basis. Visibility stacking is performed on the faint sources of known positions, and the stacked visibility data is applied to the original visibilities where self-calibration then takes place. An example of this approach in the literature is that by Radcliffe et al. (2016).

Radcliffe et al. (2016) performed stacking on visibilities of multiple faint target sources across the observed field, the stacking resulted in a single point source of higher SNR visibility data, and also applicable for self-calibration. The resultant stacked data set is applied to the original data set, and self-calibration is performed, this method is known as Multi-Source Self-Calibration (MSSC). The method has been tested on 1.6 GHz wide field very long baseline interferometry (WF-VLBI) data set, observed with the European VLBI network array, and it has been shown to increase SNR compared to standard methods (see, Figure 2.9).

2.6 Key challenges in employing stacking with the next-generation telescopes

Although stacking is a powerful technique for studying sources below the noise threshold level, there are still challenges that come with employing stacking on the next-generation telescopes like the MeerKAT, ASKAP and other SKA pathfinders, which include:

i. archiving the visibility data - long observations and large bandwidths lead to storage, and computational processing challenges for big interferometric arrays. In that case, most of the raw and calibrated visibility data will not be archived, at least not for long term storage. There are some suggestions that (a) visibility stacking could be done in real-time and the calibrated visibility data will not have to be archived for a long-term period, but for a short term period needed for the processing of (large) surveys; and (b) ensure that the visibility data to be averaged before archiving, since it will result in greater flexibility during the processing (Knudsen et al., 2014). Another alternative to reducing the data sizes is by observing for a short time and narrow frequency intervals, but this approach will result in smearing effects discussed in Section 1.2.2;

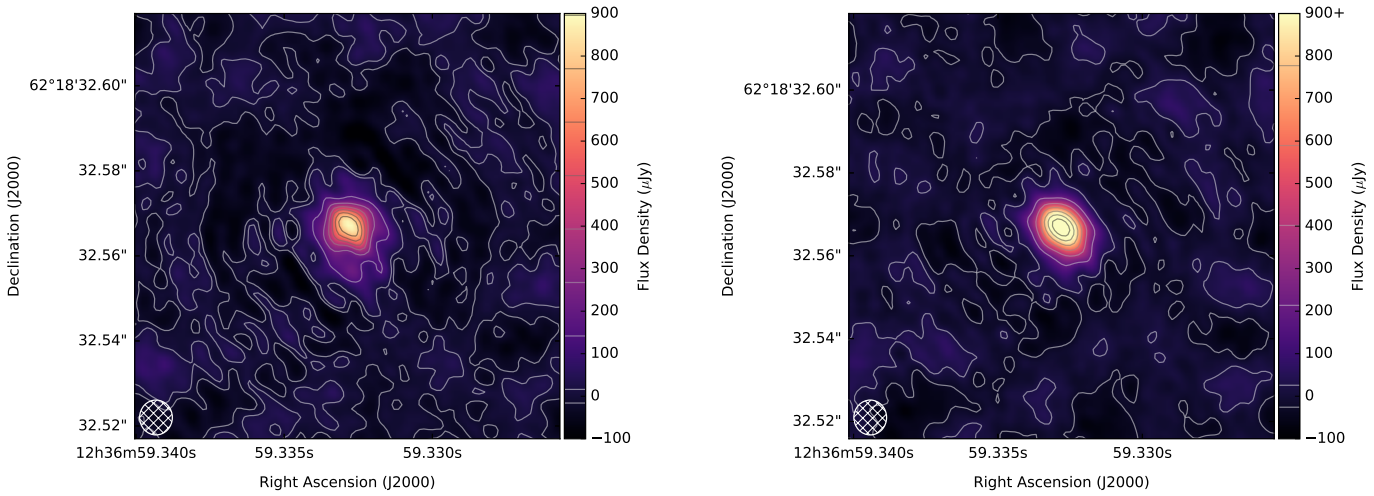

FIGURE 2.9: Image-plane comparison of standard calibration (**left panel**) and MSSC (**right panel**) results, the colour scales are the fixed for better comparison, The comparison illustrates the effect of MSSC on source structure, flux and noise levels. (**left panel**) has a flux density of 1.35 mJy while (**right panel**) has 1.73 mJy with improved SNR and noise levels. Figures are directly reproduced from Radcliffe et al. (2016).

ii. bright sources - the sensitivity of these telescopes will result in bright sources to be easily detected, and impacting the required dynamic range, therefore the stacking negatively if there are any calibration errors present. The bright sources can be subtracted by modelling their flux density distributions to attempt to ensure that the stacked results are robust. However, in most cases, residuals from bright sources will always be present, depending on the depth of the CLEANing or the quality of the visibility data (see Figure 2.3). In GHz frequencies many sources have very complex morphologies, making it difficult to model their flux distributions (Knudsen et al., 2014);

iii. source confusion - (Condon and Ransom, 2016). telescopes of very high sensitivity will result in source confusion, where sources are so crowded that one beam may contain multiple or overlapping sources, and making stacking results degenerate and ambiguous. The source confusion results in the double-counting of sources during stacking or target source is contaminated by the flux density from nearby sources, therefore giving incorrect stacking results.

Chapter 3

Methodology

3.1 Simulated observations

Stacking analyses in this thesis are performed on realistic synthetic data mimicking MeerKAT observations. The data are generated using a suite of scripts based on SIMUCLASS[1], SIMMS[2], MEQTREES '[3] and WSCLEAN (Offringa et al., 2014). The code together with the documentation can be found here https://github.com/thatoeugine/AutoStacker.git, and a summary of the documentation can be found in Appendix A. The code takes as input a catalogue of sources which is used to generate a sky model image. The observation parameters (e.g., start time, duration, bandwidth, time & frequency) are used to generate an empty Measurement Set (MS), which has thermal noise added using measured MeerKAT SEFDs. The sky model image is then Fourier transformed to generate corresponding visibilities (see Figure 3.5, for a basic flow illustration of how the data is generated). The definitions of terms that will be used in this chapter are listed in Table 3.1.

TABLE 3.1: Basic definitions of synthetic data

Sky Model catalogue	A sample catalogue of SFGs from the Tiered Radio Extragalactic Continuum Simulation (T-RECS) catalogue by Bonaldi et al. (2018).
Sky Model image	A model image consisting of sources from the sky model catalogue.
Ground truth stacked image	Median image stacked product of the sky model image (i.e., *uv*-sampling not applied).
Stacking positions	Positions of the target sources.
DATA	MS column that contains original visibility data from when the MS was created or filled.
MODEL DATA	MS column that holds Fourier transformed visibilities of a particular sky model image
CORRECTED DATA	MS column holding calibrated visibility data

3.1.1 Sky Model generation

The sky model image and its source catalogue (which will be referred to as the sky model catalogue) are generated using a SIMUCLASS task DOSKYMODEL, where SIMUCLASS is a pipeline for simulating radio interferometric data, from a model

[1] https://bitbucket.org/itrharrison/simuclass
[2] https://github.com/SpheMakh/simms
[3] http://meqtrees.net/

image to deconvolved images, built-in support of the SuperCLASS experiment: http://www.e-merlin.ac.uk/legacy/projects/superclass.html.

The sky model consists of sources from the Tiered Radio Extragalactic Continuum Simulation (T-RECS), a realistic simulation of the radio continuum number counts by Bonaldi et al. (2018). The simulation consists of catalogues of two main radio continuum source populations namely, SFGs and AGN, with luminosity, flux density, coordinates, size and shape information. The structure of the SFG catalogues are shown in Table 3.2, indicating information for each column of the catalogue. The catalogues are separated into three categories: (i) the deep field with FoV = 1 deg^2, (ii) the medium field with FoV = 25 deg^2, and (iii) the wide-field catalogue with FoV = 400 deg^2. The T-RECS simulations have proven to be realistic, to the level required for this project, with their luminosity functions and differential source counts agreeing very well with literature data at 1.4 and 3 GHz frequencies, examples of which are shown in Figures 3.1 and 3.2.

TABLE 3.2: Structure of the T-RECS SFG catalogues. Table is reproduced directly from Bonaldi et al. (2018).

Column	Tag Name	Units	Description
1	logSFR	$\log_{10}(\frac{M_\odot}{yr})$	SFR
2:19	I_{freq}	mJy	Total intensity flux density of the source at frequency *freq*
20:37	P_{freq}	mJy	Linear polarized flux density of the source at frequency *freq*
38	Mh	$\log(M_\odot)$	Dark halo mass
39	x_coord	deg	First angular coordinate for the flat-sky approximation
40	y_coord	deg	Second angular coordinate for the flat-sky approximation
41	latitude	deg	Latitude spherical coordinate for a chosen centre of the field
42	longitude	deg	Longitude spherical coordinate for a chosen centre of the field
43	redshift	none	redshift
44	size	arcsec	Projected apparent size of the disc
45	e1	dimensionless	First ellipticity component
46	e2	dimensionless	Second ellipticity component
47	PopFlag	dimensionless	Number identifying the sub-population: 1, 2, 3 for late-type, spheroidal and lensed spheroidal galaxies, respectively.

Figure 3.1 presents the comparison between T-RECS and literature's (as indicated on the legend in colour) differential source counts at 1.4 and 3 GHz. The total counts agree very well with the real data from the literature for both AGN and SFGs. The figure mostly reproduces the differential source counts at 1.4 and 3 GHz, where we will be stacking. The stacking range (mostly 1 – 1000 μJy) is dominated by SFGs, which is the only population we will be concentrating on, not AGN. Figure 3.2 compares the radio luminosity functions of T-RECS to literature (indicated on the legend) at 3 GHz for SFGs, the comparison shows a good agreement. This shows a range of

luminosities that T-RECS covers.

In this thesis, the deep field catalogue is used to generate the sky model by randomly selecting $\sim$ 2 million SFGs within a FoV of 0.75 x 0.75 deg^2 with a low flux density cut of 0.1 μJy, exponential galaxy profiles, disc sizes of range 0.003 $\leq$ size $\leq$ 41.361 arcseconds. The pointing centre is selected as Right Ascension (RA) 00h00m00s and Declination (DEC) -30d00m00s in epoch J2000, the latter providing near-zenith observation for MeerKAT when sources cross the prime meridian. After a range of experimentations, the sky model image is generated at S-band frequency (3 GHz) with bandwidth 256 MHz split into 16 channels each of width 0.209 MHz. These choices are motivated by the the desire for accurate, realistic interferometric tests, while remaining pragmatic of processing time. The resultant image is of size $\sim$ 27 000 x 27 000 pixel^2 with a scale of 0.1 arcsec per pixel. A brief description of the sky model generation is shown in Table 3.3.

TABLE 3.3: Sky Model information.

Pointing Centre	RA: 00h00m00s DEC: -30d00m00s Epoch: J2000
FoV size	0.75 x 0.75 degrees^2
Low flux cut	0.1 μJy
Galaxy profile	Exponential
Disc sizes	0.003 $\leq$ size $\leq$ 41.361 arcsec
Number of sources	$\sim$ 2 million
Observed frequency	3 GHz
Total bandwidth	3.34 MHz
Channel width	0.209 MHz
Number of Channels	16

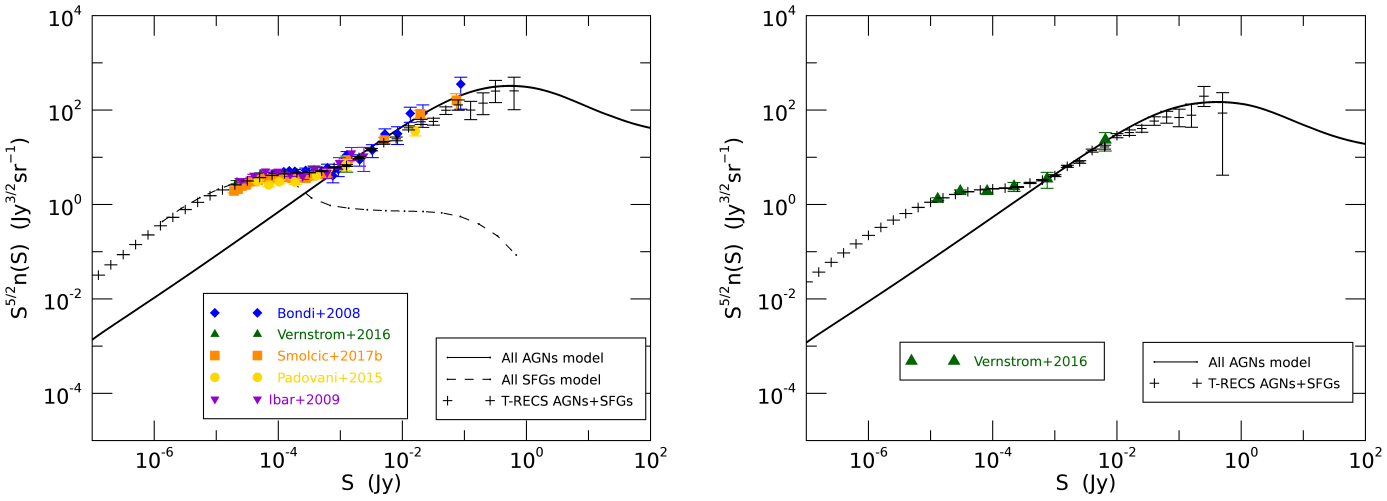

FIGURE 3.1: Comparison of T-RECS and literature's differential source counts as a function of total intensity for both SFGs and AGNs at frequencies 1.4 GHz (**left**)and 3 GHz (**right**). Figures are directly reproduced from Bonaldi et al. (2018).

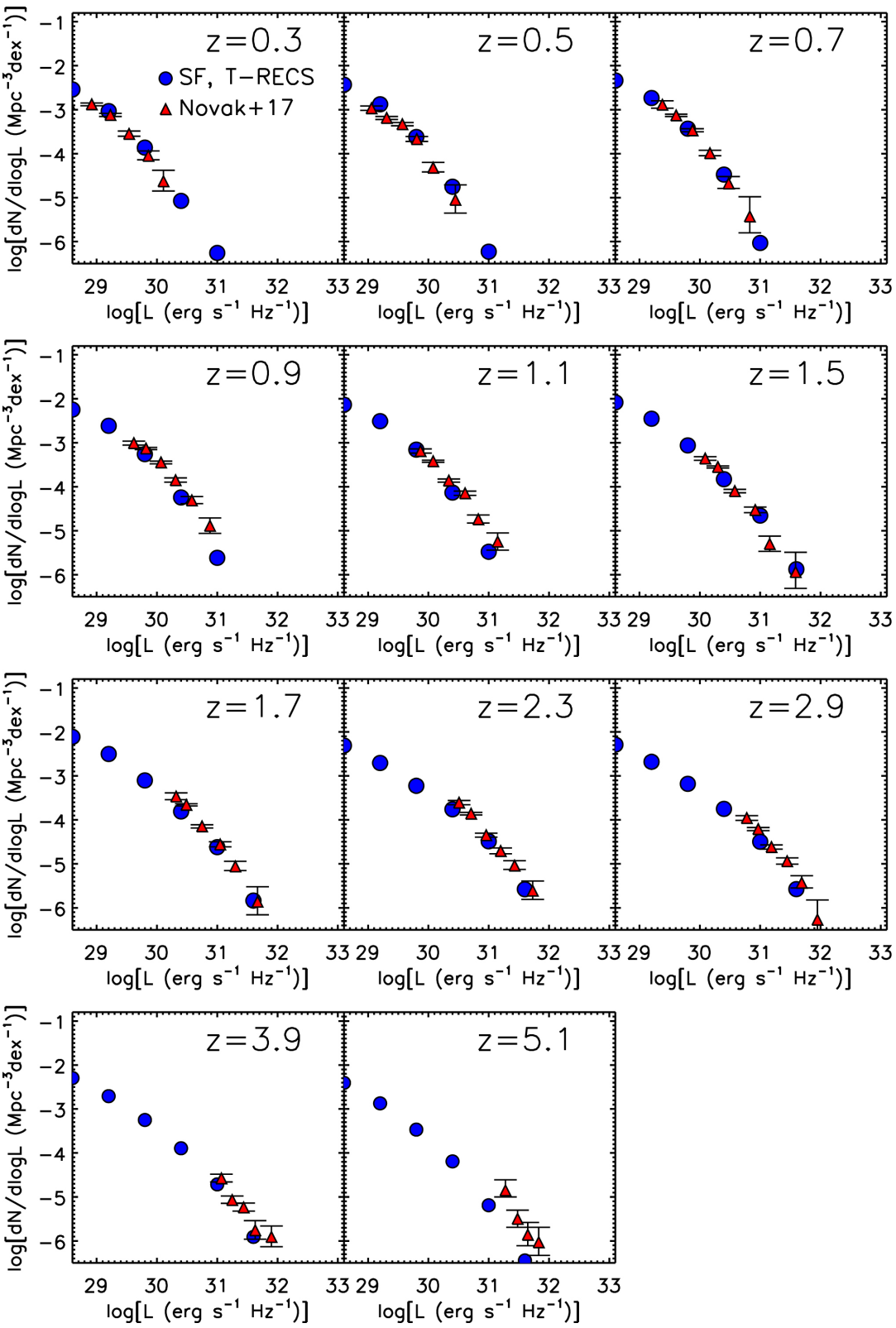

FIGURE 3.2: Comparison of T-RECS and literature's Radio Luminosity Functions (RLFs) for SFGs at 3 GHz frequency. Reproduced directly from Bonaldi et al. (2018).

3.1.2 Simulated MeerKAT observations

The observations are conducted using 64 antennas for an observation length of 1 hour, recording visibilities at an integration time of 8 seconds and adding thermal noise based on a per antenna SEFD of 450 Jy for an S-band feed. See Table 3.4 for a brief description of the MeerKAT's simulated observations. While this does not correspond to a typical observation mode, the choice of parameters is driven in part by the speed of processing due to the lower sky density, FoV, and primary objective in this thesis of performing a basic comparison of image-vs-visibility-plane stacking for MeerKAT observations. The MeerKAT S-band SEFD is assumed to be $\sim$ 450 Jy, which is similar to the L-band SEFD as indicated by early S-band receiver tests on-site. While this number is not exact and will also be frequency-dependent across the band in practice, it suffices within the scope and objectives of this MSc thesis. The simulated observations are generated using SIMMS, a software package written predominately in PYTHON that uses a CASA simulation tool to generate empty MS. MEQTREES, a software package for implementing the RIME to write visibilities into an MS. The *uv*-coverage of the MeerKAT observation is shown in Figure 3.3, showing high sensitivity for the detection of small and large structure sources.

TABLE 3.4: Observations data information for MeerKAT's simulations.

Pointing Centre	RA: 00h00m00s DEC: -30d00m00s Epoch: J2000
Centre frequency	3 GHz
Total bandwidth	3.34 MHz
Channel width	0.209 MHz
Number of Channels	16
Averaging time	8 s
Number of Antennas	64
Observation time	1 h
SEFD per antenna	450 Jy

Using the WSCLEAN task PREDICT, the sky model image is converted into visibilities that are then inserted into the MODEL DATA column of the MS. The CASA task UVSUB is used to add the predicted visibilities from the MODEL DATA into the DATA and CORRECTED DATA columns. The resultant MS is of a MeerKAT simulation at S-band. The visibility prediction by WSCLEAN is tested by comparing a deconvolved image from the predicted visibilities (a simulated MeerKAT image of the sky model) with the sky model image smoothed with MeerKAT's PSF, and the comparison images are shown in Figure 3.4, showing good agreement and well suited to the objectives and scope of this thesis.

3.2 Stacking

3.2.1 Image stacking

With the sky model simulation and MeerKAT simulation in place, we now move toward the stacking component. The image stacking procedure is performed on the sky model image by extracting 101 x 101-pixel^2 postage stamps centred on each

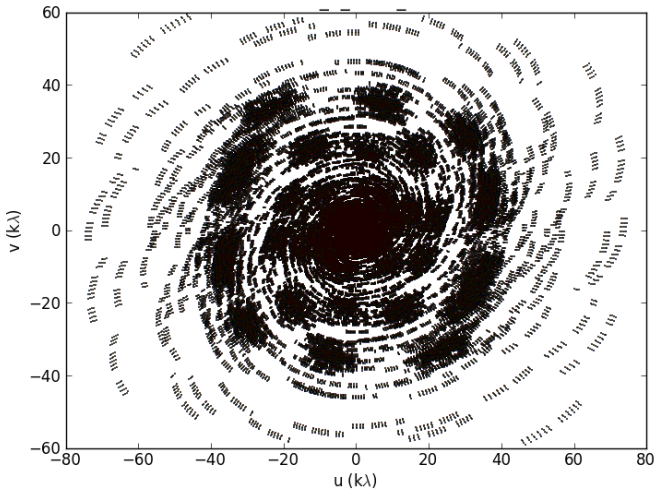

FIGURE 3.3: MeerKAT's S-band simulation *uv*-coverage (i.e. sampling function of the Fourier plane). The units are in kilo-wavelength for S-band observations, with shortest baseline being 20 m and the longest is 8 km.

sky-model catalogue position, the postage stamps are then combined on a pixel-by-pixel basis using the median stacking method. We refer the reader to Section 2.2, for pixel-by-pixel stacking procedure in detail and Figure 3.5 for a simple flow diagram illustration of the stacking method used. The resultant image is a median stacked image referred to as the Ground-Truth image because the image represents the true flux densities from the input stacked sources (i.e. the image does not have clean artefacts and missing Fourier components). Uncertainties on the Ground-Truth (GT) image are calculated using the Mean Absolute Deviation (MAD) approach (e.g., Zwart et al. (2014)),

$$\sigma_{<x>} = \frac{\sigma_{\overline{x}}}{1.4826} \tag{3.1}$$

where $\sigma_{\overline{x}} = \frac{\sigma}{\sqrt{n}}$, σ is the standard deviation and n is the sample size (i.e., the number stacked objects). This MAD expression is used to calculate the pixel uncertainties of stacked images on a per pixel basis.

3.2.2 Visibility stacking

We compare image stacking results to visibility stacking by performing a range of visibility stacking experiments varying parameters such as the stacking depth, CLEAN depth and the maximum distance from the phase centre. This allows testing where the visibility stacking approach is more effective and feasible than the traditional image stacking approach as well as measuring its limitations. The visibility stacking approach is performed on the MeerKAT simulated data discussed in Section 3.1.2. The visibility stacking is performed with an algorithm developed by Lindroos et al. (2014), where for the input target positions the visibilities are combined by phase-rotating the visibilities to each input stack position using the mean. This results in single visibility stacked data set (MS) that can also be imaged for comparison with the image stacking results. However, in this thesis, the comparison is

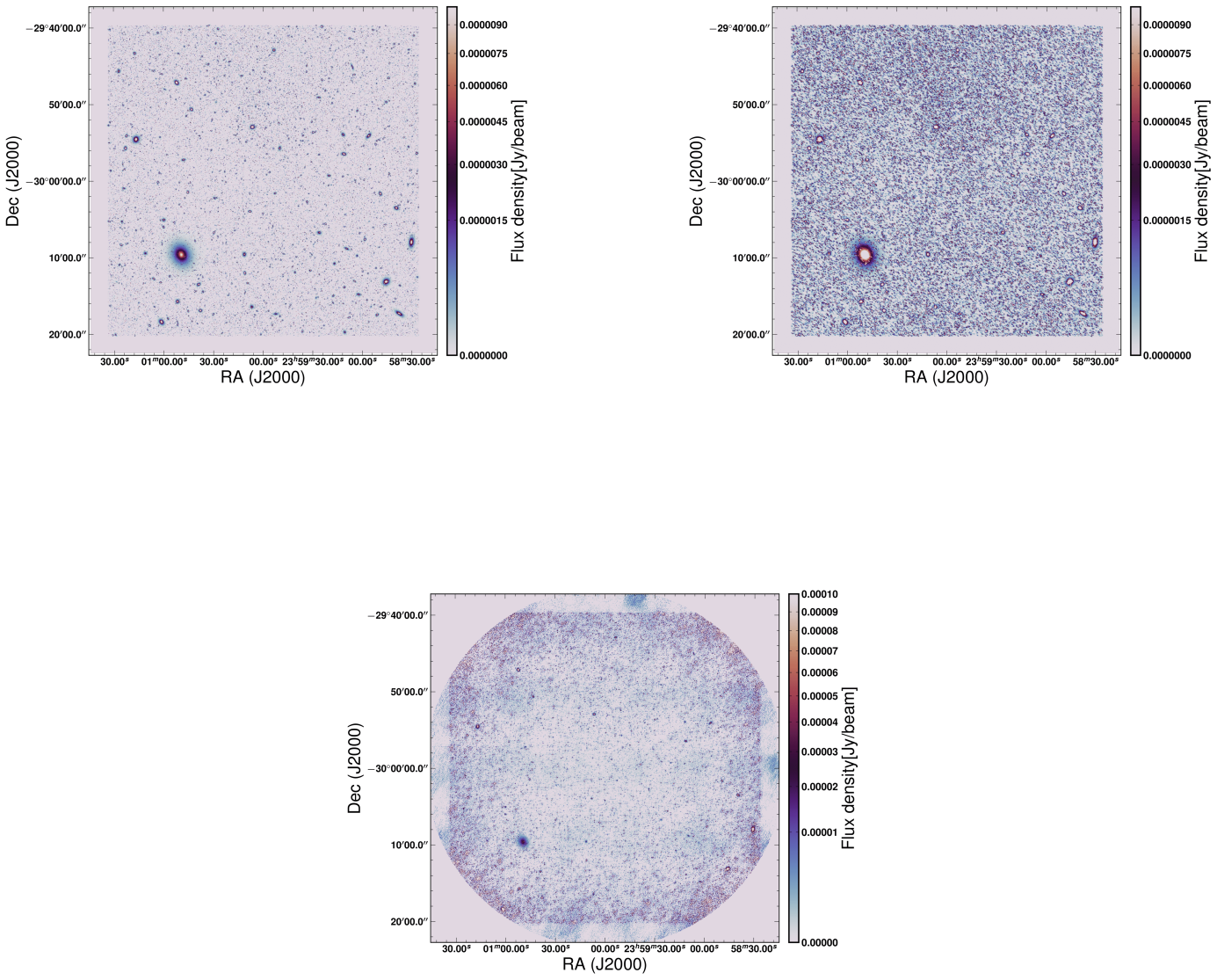

FIGURE 3.4: **Top left panel**: Sky model image sampled from the T-RECS SFGs catalogue by Bonaldi et al. (2018), the image is generated using the SIMUCLASS code; **top right panel**: the sky model image smoothed with a Gaussian of the same size as MeerKAT's PSF of BRIGGS weighting; **bottom panel**: Simulated MeerKAT image of the sky model in the top left panel. Both images are shown on the same scale for better comparison.

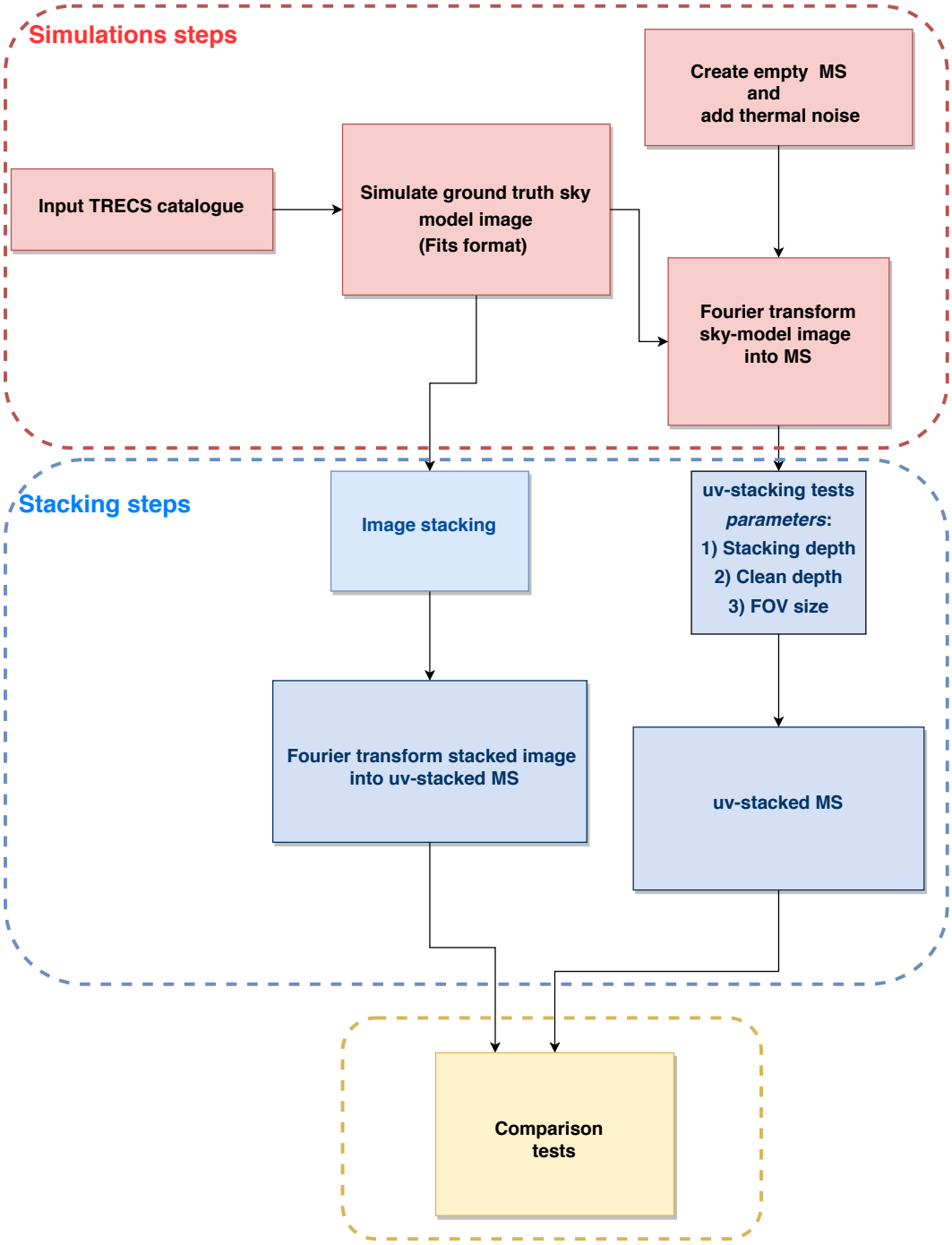

FIGURE 3.5: Schematic diagram of how the analysed data is generated. The orange border indicates the steps of the simulation; the blue indicates the stacking steps and the yellow indicates the comparison tests.

made by extracting raw visibility data of the resultant stacked data and using a similar comparison approach as in Lindroos et al. (2014), by plotting the real component visibilities as a function of *uv*-distance. See Section 2.3, for a more detailed description of the visibility stacking procedure. The systematic comparisons for each varied parameter are discussed below.

Stacking depth

For the stacking depth experiments, we want to determine a suitable number of target sources to stack per resolution element, to avoid source confusion dominating results as discussed in Section 2.6. The stacking is performed on a MeerKAT single-pointing dataset for a different number of resolution elements per source of 100, 50, 30, 15 and 5 with the same fixed area. Stacking depth is based on the$\sim$ 2 million simulated SFGs over 25 deg^2 (see Section 3.1.1) divided by the number of resolution elements per source. The resultant ratio is rounded to the nearest whole number, an example of this is shown in Figure 3.6.

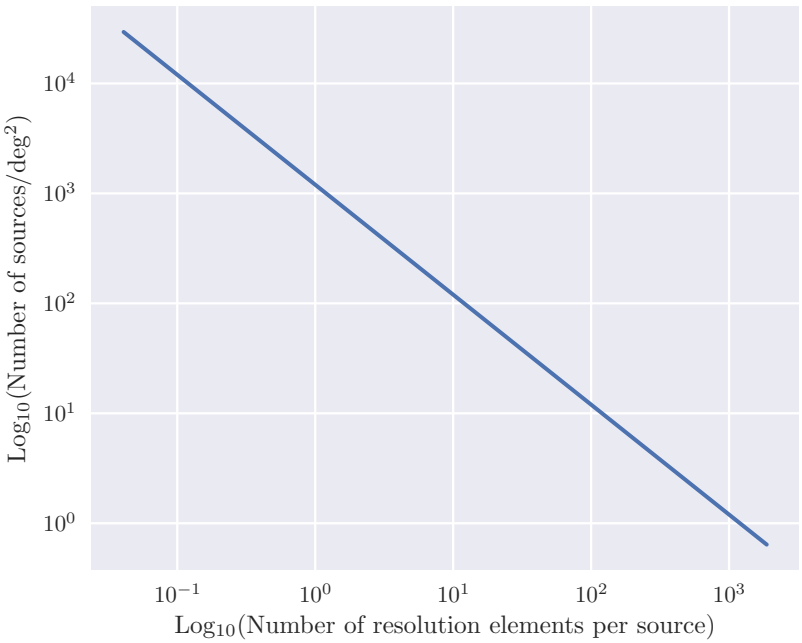

FIGURE 3.6: Stacking depth, a plot of a number of sources per square degree as function of the number of MeerKAT resolution elements per source. The number of sources per square degree drops with respect to an increase in the number of resolution elements per source.

CLEAN depth

The CLEAN depth parameter explores how deep we need to subtract out bright sources that may contribute as noise towards nearby faint target sources to get a robust stacking detection. For this procedure, a suitable stacking depth and area are fixed. Unwanted bright sources are then modelled and removed from the visibility data as follows. A model data set of all sources in the original data set is produced by imaging using a CASA task CLEAN. The bright sources are cleaned down to a

flux density threshold of 10, 1, 0.1 and 0.01 mJy/beam, and also varying the BRIGGS weighting parameter by -1, -0.5, 0, and 0.5 for each clean flux density threshold. The resultant model *uv*-data of bright sources is subtracted from the original *uv*-data to produce a residual *uv*-data set, where stacking is performed using input stack positions. More details are described in Section 4.

Maximum phase centre offsets

For the maximum distance from the phase centre, seek to better understand how far from the phase centre we can stack, to minimise a decrease in flux density due to time and bandwidth smearing and the primary beam. For this parameter, stacking is performed on target sources within a maximum distance of 25%, 50%, 75% and 100% from the phase centre, also with a suitable stacking depth and CLEAN depth fixed, as detailed in Chapter 4.

Chapter 4

Discussion of results

In this chapter, we present a suite of *uv*-stacking results using the method discussed in chapter 3, as well as on real MeerKAT data. As already be clear from previous chapters and based on previous work, the parameter space one can explore in comparing image and visibility-plane stacking is large. Within the scope of this MSc thesis, the objective is to provide a selected set of indicative and illustrative stacking experiments that may inform future research activity in this area.

In the literature, previous stacking experiments for studies of faint radio sources (e.g., Lindroos et al., 2014) did not include the following parameters when performing *uv*-stacking: the stacking depth, CLEAN depth and the maximum distance from the phase centre. Each of these parameters was discussed earlier in Section 3.2.2. They are important to explore visibility stacking results in a MeerKAT context, and all the complexity its particular set of specifications bring. Previous stacking experiments were mainly focused on removing bright sources, and wide-field effects, which involves stacking sources spread far from the phase centre. Therefore, this thesis tries to close that gap on the MeerKAT application.

4.1 Interferometric Simulation Results

4.1.1 Stacking depth

A key parameter in stacking is the number of beams per source. The *uv*-stacking of MeerKAT data for all the ~ 2 million simulated SFGs over the designated solid angle would fail since the telescope can only hold 1 million sources for its 1 million beams, therefore we would be double-counting the sources during the stacking procedure over the 25 deg^2 FoV. This requires an array of higher resolution, e.g. the VLA-A configuration, but in our case, the appropriate stacking depth is explored. Figure 4.1, on the left panel, shows the GT image, which is our target flux density ($\sim 3.4 \pm 0.012$ nJy) to be recovered, the image is smoothed with MeerKAT's PSF for better comparison with expected stacking results, and on the right panel is the flux density distribution of the ~ 2 million simulated SFGs. This shows that the majority of the SFGs have flux density less than 0.1 μJy.

We conduct two different simulations, one where no bright sources are included and the other where the brightest 100 sources are included, to compare real and idealized bright source subtraction. The two simulations are conducted for four of the different stacking depths discussed in Section 3.2.2. The stacking is limited to target sources below the image noise level of 5.54 μJy (`robust = -0.3`), in order to increase the chances of recovering the GT flux density, the target sources are selected at random, and they are of flux density less than 0.1 μJy.

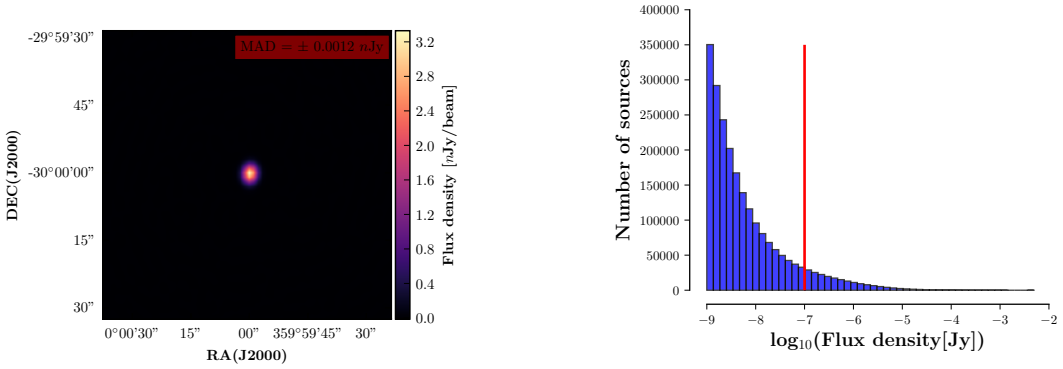

a b

FIGURE 4.1: **(a)**: Ground-Truth image of the $\sim$ 2 million simulated SFGs, the image is smoothed with MeerKAT's PSF for better comparison. The image has a peak flux density of about $\sim$ 3.4 nJy and uncertainty of $\pm$ 0.012 nJy, using the MAD. **(b)**: Distribution of flux density for the simulated sources. The target flux density is on the left side of the red solid line (i.e., sources of flux density less than 0.1 μJy) and the flux densities on the right-hand side are considered as noise.

In Figure 4.2, we show *uv*-stacked results for simulations with no bright sources (i.e., $<$ 0.1 μJy, first column) and where bright sources are included (second column), for two different stacking depths. The first row represents a stacking depth of $\sim 2.1\times10^4$ target sources and the second row $\sim 4.3\times10^5$ target sources. The bright sources are cleaned down to a flux density threshold of 0.01 mJy/beam. For simulations with no bright sources, there is a clear detection at the phase centre, with the peak flux density increasing with respect to the stacking depth and this is due to the overlapping (within one MeerKAT PSF) leading to double counting during stacking. Where bright sources are included, there is no detection, but just noise due to inaccurate subtraction of the bright sources. This demonstrates the fact that bright sources impact stacking results negatively, resulting in no detection at the phase centre of the image stacked results and therefore for MeerKAT data newly improved CLEAN methods are required for a more accurate subtraction of bright sources if deep stacking experiments are required with MeerKAT.

Further stacking experiments are conducted by only focusing on simulations with no bright sources, i.e., we assume perfect bright sources removal before stacking. From that, a suitable stacking depth is chosen by estimating the integrated flux of the four different stacking depth *uv*-stacked results. We use a CASA task IMFIT to estimate the integrated flux. This task estimates source parameters by fitting one or multiple Gaussian components, and it requires imaging of the *uv*-data, of course. The same approach is taken in the real data example in this chapter. The estimated integrated flux via IMFIT are shown in Table 4.1. The estimated integrated flux is divided by the GT flux density; the ratio that is closest to 1 is in principle the most suitable stacking depth. Therefore from Figure 4.3 the 15 number of resolution elements per source corresponding to $\sim 1.45\times10^5$ target sources seems to be the closest to 1 but closer, qualitative inspection suggests caution in assuming an accurate stack for this example. The problem might be due to inaccuracy of model fitting on a model since the imaged data is a model representation of the *uv*-data. Therefore, in this case, the second nearest to 1, which is the 100 resolution elements per source is chosen instead. The size of the data points indicates the stacking depth, meaning small data

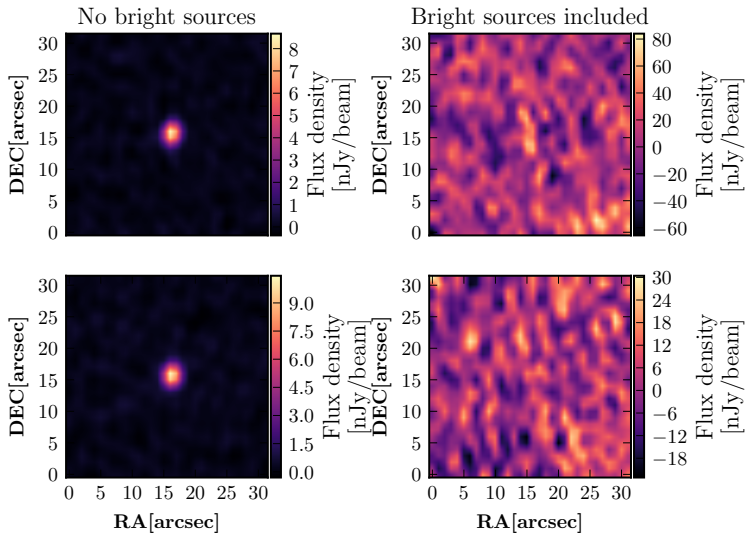

FIGURE 4.2: uv-stacked results for different stacking depth simulation where there are no bright sources (**first column**) and where bright sources are included (**second column**). The first row represents stacking depth of $\sim 2.1\times10^4$ sources and the second $\sim 4.3\times10^5$ sources; with 100 and 5 number of resolution elements per source respectively.

point, small stacking depth and large data, large stacking depth.

TABLE 4.1: Estimated flux density for different stacking depths.

Stacking depth (Number of resolution elements per source)	**Integrated flux density (nJy)**
100	6.19 ± 0.26
50	9.08 ± 0.24
30	6.64 ± 0.24
15	3.36 ± 0.26
5	12.5 ± 0.54

In Figure 4.4 we show a distribution of (a) flux density, and (b) source size, for the suitable stacking depth of $\sim 2.1\times10^4$ target sources (i.e., 100 number of resolution elements per source). The distributions show that the stacking depth has sources of flux density of 1 – 100 nJy, which supports that the correct selection was made, and source sizes of 0.0032 – 1 arcsecs.

4.1.2 CLEAN depth

After finding a suitable stacking depth, we performed stacking within a fixed S-band FoV of 0.42x0.42 degrees^2. This section explores varying the clean threshold of bright, foreground sources from 0.01 – 10 mJy. Real deconvolution is performed (i.e., we actually cleaned the image map), however, this assumes perfect calibration. From the stacking analysis, we extracted the real component visibility amplitude and compared them to those of the GT. The real values of the flux density amplitudes are averaged in *uv* bins, see Figure 4.5. We find that results are not affected by

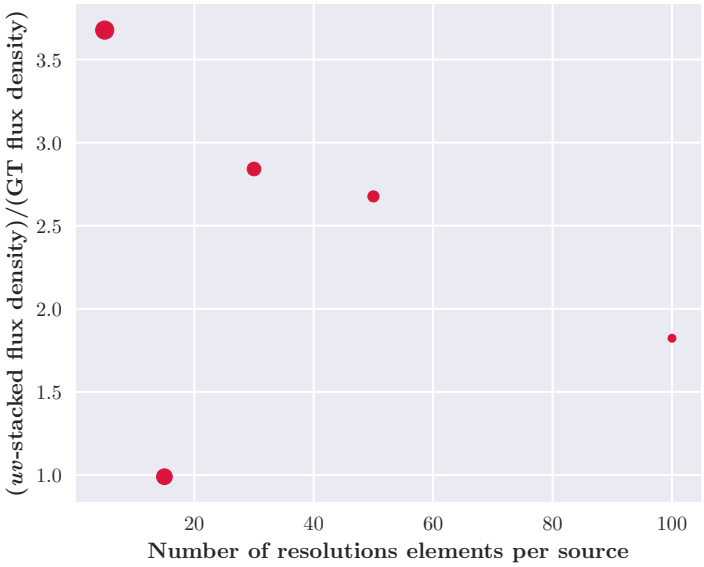

FIGURE 4.3: Flux density as function of the number of resolutions elements per source, each data point indicate the individual resolution elements per source (100, 50, 30, 15, 5) where sizes indicates the number of sources for each resolution element, meaning the big data point has more sources.

the clean threshold as expected, i.e., the four curves are virtually coincident, however, the visibility stacked values show a clear upward bias compared to the GT.

The clean depth stacking experiment is explored in more detail by varying the BRIGGS weighting robust parameters for a fixed clean threshold of 0.01 mJy. In Figure 4.6, we show the stacking analysis where we extract the real visibility components for robust parameters of -1.0, -0.5, 0 and 0.5 as indicated by the legend and compare them to those of the GT. From that, we can see that even when changing the robust parameter stacking results are still not affected, mainly because the target sources are still below the clean threshold and perfect calibration is assumed. This will not be the case in practice but its exploration is beyond the scope of this thesis.

4.1.3 Maximum phase centre offset

Finally, the CLEAN depth of (0.01mJy/beam and -0.5 robustness) and stacking depth (2.1×10^4 target sources) are fixed on this set of experiments, and only the maximum allowed distance of sources from the phase centre is varied by 25%, 50%, 75% and 100%. Sources outside that distance are excluded from the simulations. From the stacked results, we extract the real component visibility amplitude and compare them to those of the GT, averaged in *uv* bins, see Figure 4.7. The 100% and 75 % distance from the phase centre stacks show no change in the recovered flux just like in the previous stacking experiments; this is due to the stacking depth being very similar. However, the 50% and 25 % distance stacks show a slight decrease in the recovered flux density, with 25 % distance from the phase centre stack being the closest the GT, with 2 orders of magnitude.

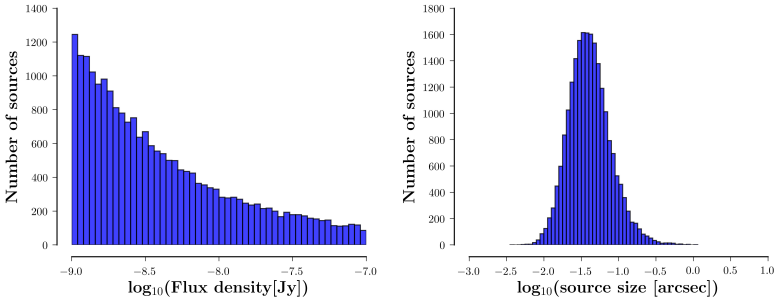

(a)

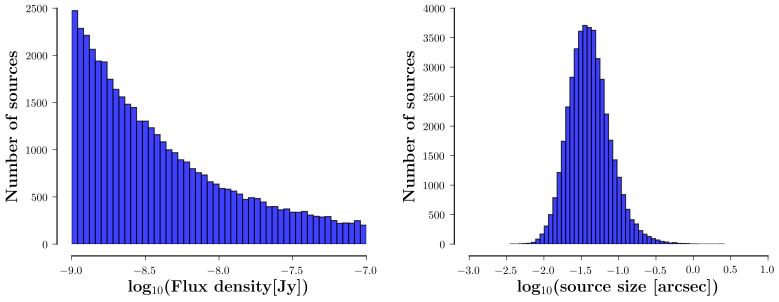

(b)

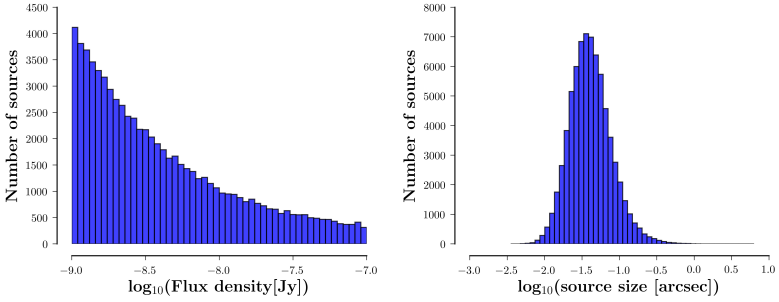

(c)

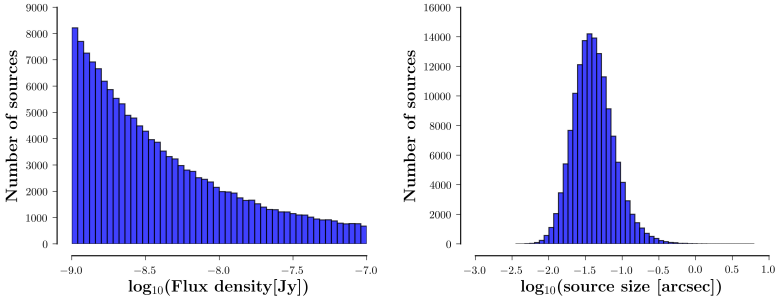

(d)

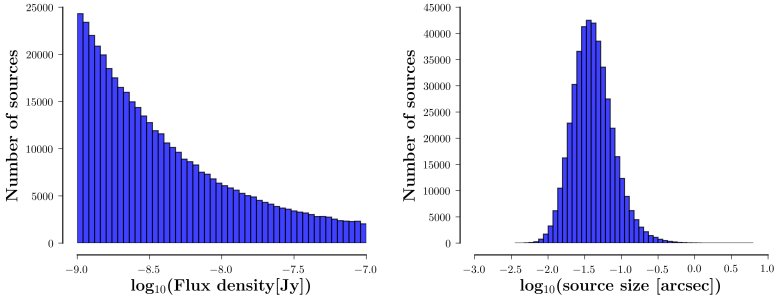

(e)

FIGURE 4.4: The distribution of flux density and source size for 100 **(a)**, 50 **(b)**, 30 **(c)**, 15 **(d)** and 5 **(e)** number of resolution elements per source. The flux density for 100 number of resolution elements per source ranges from 1 – 100 nJy and the source size from 0.0032 – 1 arcsecs

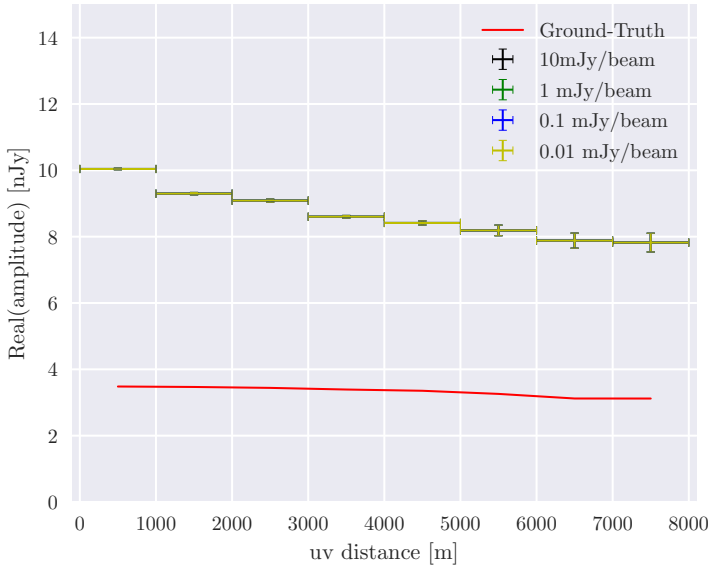

FIGURE 4.5: Stacked as a function *uv*-distance. The flux density is averaged *uv*-distance bins, taking the real part of the visibility amplitude. Uncertainties are defined as the standard deviation within each bin. The plot combines data from different clean thresholds. The red curve indicates the same for the Fourier transformed ground truth, showing a clear bias once again.

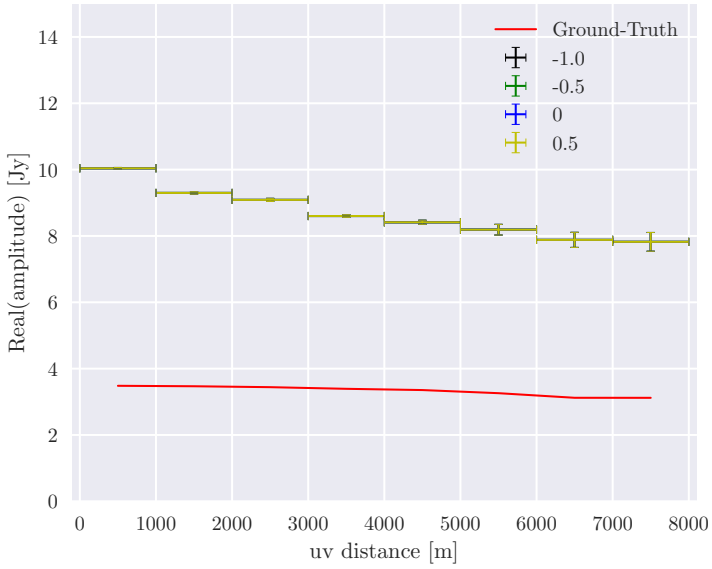

FIGURE 4.6: Stacked visibilities as a function *uv*-distance. The flux density is averaged *uv*-distance bins, taking the real part of the visibility amplitude. Uncertainties are defined as the standard deviation within each bin. The plot combines data from different BRIGGS weighting robust parameters. The red curve indicates the same for the Fourier transformed ground truth, showing the bias does not stem from imaging weights.

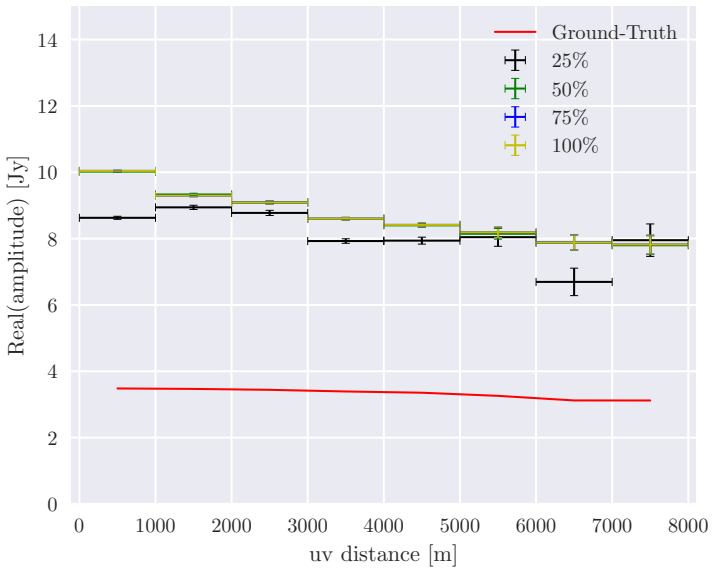

FIGURE 4.7: Stacked visibilities as a function *uv*-distance from the offset from phase centre test. The flux density is averaged *uv*-distance bins, taking the real part of the visibility amplitude. Uncertainties are defined as the standard deviation within each bin. The plot combines data from different maximum distances from the phase centre. The red curve indicates the same for the Fourier transformed ground truth.

4.2 Application to Real MeerKAT Data

In this section, we demonstrate the application of *uv*-stacking on real MeerKAT data. The objective is to demonstrate a feasible use case for visibility stacking with this interferometer. Within the simulated, high-source density applications described in Section 4.1, it is clear that as soon as visibility stacking is applied to data with a high density of sources, the results show contamination by the short baselines, which very rapidly hit the confusion limit and/or adversely affected by imperfect deconvolution. This demonstrates a clear limitation to visibility stacking in a MeerKAT context when compared to previous applications with very sparse source densities, such as ALMA observations at millimetre wavelengths and sub-arcsecond angular resolution where source densities are orders of magnitude lower. Therefore, in selecting an application to highlight in this thesis, careful thought had to be applied to that which would be appropriate. There were two requirements: the stacking application had to reveal emission below the detection threshold, while at the same time not so deep as to encounter the source-density challenges previously demonstrated.

The decision was therefore made to perform continuum stacking on an ensemble of galaxies in the Abell 3408 galaxy cluster. These galaxies were selected by their neutral hydrogen (HI) content, as detected by MeerKAT. All HI-detected objects were included in the sample, a map of which is shown in Figure 4.8. The scientific objective is to measure the average star formation rate of these HI-selected galaxies, as probed by their aggregate radio continuum luminosity, under the assumption that clear AGN sources are excluded. To assist in this, different subsamples will be

stacked, including one where all sources in the HI-selected sample with clearly detected radio continuum emission are removed from the sample, which may mitigate AGN contamination to some extent.

The science goals of this stacking process, specifically the visibility stacking are numerous and covered in a publication describing the MeerKAT HI observations of Abell 3408 (Blecher et al., in prep.). Briefly, it has long been known that rich galaxy environments like clusters can result in galaxy transformation, either through merger activity or ram-pressure stripping as the sources move through Intra-Cluster Medium (ICM, e.g. Gunn and Gott 1972). This can result in compressed, distorted, or even completely stripped HI within galaxies in these environments. At the same time, this process can also lead to enhancement in or quenching of star formation. Since many of the lower mass objects are barely resolved by MeerKAT at $z \sim 0.05$, visibility stacking can tackle several of these questions at once. Firstly, the stacked radio continuum will enable an aggregate star formation rate estimate of low-SFR galaxies. Secondly, as has been shown in the literature, the visibility-domain stacking enables a far more robust measure of the marginally-resolved size of lower-mass objects, which will be of particular relevance of future statistical measurements of the mass-diameter relation below the detection threshold.

The combination of these effects means that a statistical comparison can be made of the star formation rate, HI mass, and galaxy size - all of which are expected to be influenced in a rich cluster environment. This can then supplement the same analysis done on individual detections and described in Blecher et al. (in prep.). The subject of this thesis is primarily on demonstrating the methods, so the range of possible scientific analyses will be deliberately limited in scope and deferred for future work.

The HI-selected Sample

The map shown in Figure 4.8 has a total of 64 galaxies, with HI masses that range between $\log(M_{\rm HI}/{\rm M}_\odot) \approx 8.5 - 10.5$ (Blecher et al., in prep.). These have a maximum angular separation of ~ 47.72 arcmin from the observation phase centre, which is co-located with the Abell 3408 cluster centre.

In Figure 4.9, the location of each input galaxy is shown, coloured by its primary beam correction. We assume a circularly symmetric primary beam with full width half maximum (FWHM) of

$$\theta_b = 57.5' \left(\frac{\nu}{1.365\,{\rm GHz}} \right). \tag{4.1}$$

Since sources are in close redshift proximity to each other we assume the same frequency of 1.365 GHz for the purposes of estimating the primary beam correction. The primary beam correction is adopted from Equation (3) in Mauch et al. (2020) and approximate corrections can be seen in Figure 4.9.

We have noticed when imaging the 64 galaxies individually at their stacking positions that there is still some remaining residual continuum emission which may contaminate our stacking results. Examples of these postage stamps at stacking positions are shown in Figure 4.10, the stamps are of size 64x64 pixels, 0 mJy/beam clean flux density threshold, BRIGGS weighting with a `robust` parameter of -0.3. To

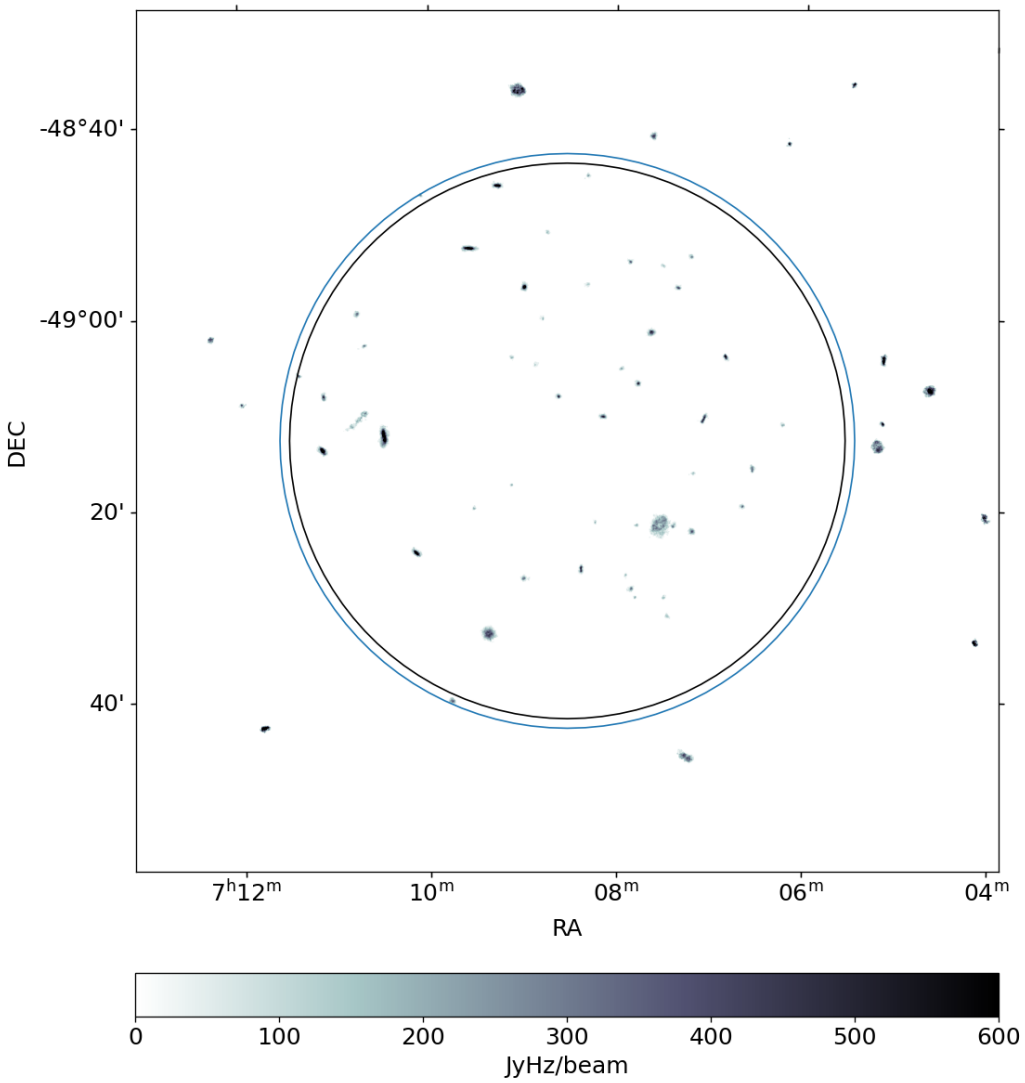

FIGURE 4.8: Reproduced HI total-intensity map from Blecher et al. (in prep.), showing the newly-discovered HI galaxies on which continuum stacking was performed in this work. The solid black line shows the MeerKAT primary beam FWHM at 1.4 GHz, while the blue shows the R_{200} radius, the distance at which the density is 200 times the critical density of the Universe. See Blecher et al. (in prep.) for further details.

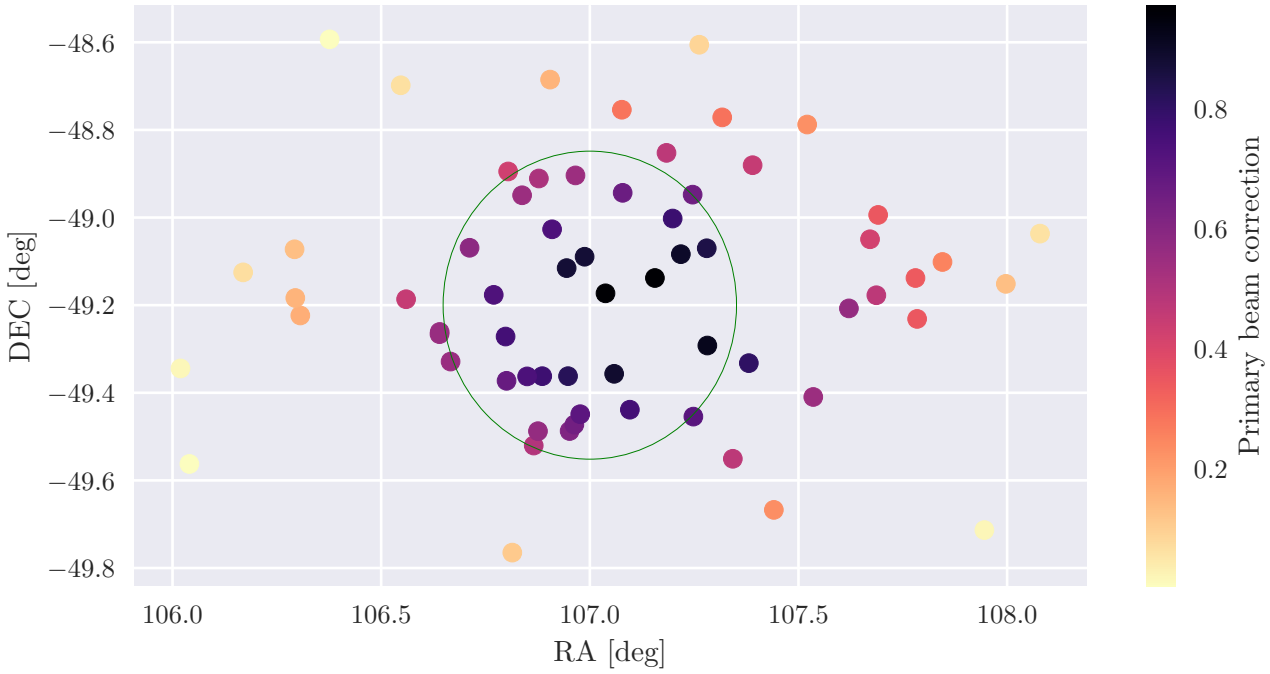

FIGURE 4.9: Coordinates of HI-sample to be stacked in radio continuum. The data points are coloured their primary beam correction. The green solid line shows half the MeerKAT primary beam FWHM/2 at 1.4 GHz

perform a more thorough stacking analysis, we split the stacking positions into five different sub-sample catalogues:

1. **Full catalogue (dirty):** this includes all 64 stacking positions, but stacking is applied on a dirty image (for image-stacking) or on a visibility data set where there is no subtraction of nearby foreground bright sources (in the case of *uv*-stacking).

2. **Full catalogue (cleaned):** this includes all 64 stacking positions, but stacking is applied on a cleaned image or visibility data set were nearby foreground bright sources have been subtracted out down to a clean flux density threshold of 10 μJy/beam.

3. **Non-contaminated fields:** For this sub-sample, positions where any detection off-centre (i.e., off from the phase centre) on $\sim$ 1 arcmin^2 postage stamps at stacking positions (e.g., stacking position 11, 12, 27, 41 and 58) are excluded from the stack.

4. **Non-Detection fields:** positions where there is a detection at the target position (e.g., stacking position 8, 20, 25, 28 and 52). These positions are excluded from the stack.

5. **Non-detect, non-contaminated:** consists of stacking positions where there is no off-centre nor centre detections in the postage stamp.

These sub-samples are selected to measure the impact of direct detections and field contaminants in the final stacked results.

Image-plane stacking results

Figure 4.11 shows the mean stacking results of an ensemble of HI-selected galaxies in the Abell 3408 galaxy cluster, for the full catalogue (dirty and cleaned) sub-samples. The same image stacking procedure, as discussed in Section 3.2.1, is applied. The colour scale of both the dirty and cleaned sub-samples stacked images have similar peak flux density of $\sim$ 14 μJy, this indicates that for image stacking, subtracting out bright sources does not change the stacking results. For both image stacking results, their corresponding residual images (right-hand side) made by subtracting a 2D Gaussian fit to the central stacked detection are included. The results for the other sub-samples are shown in Table 4.2.

Visibility-plane stacking results

As discussed previously in Section 2.3 *uv*-stacking results can be imaged and directly compared with image-stacking results, as well as through Fourier-domain component fitting (e.g. CASA's `uvmodelfit` task), however, what is important is that the stacking itself is performed in the visibility plane, for this thesis. Figures 4.12 and 4.13 show *uv*-stacking results on an ensemble of galaxies in the Abell 3408 galaxy cluster. Figure 4.12 shows *uv*-stacking results where no remaining continuum emission was cleaned out (top panel) and where the remaining emission is cleaned out down to a flux density threshold of 10 μJy/beam (bottom panel). We refer these results as Full catalogue (dirty) and Full catalogue (cleaned) respectively. From both the uv-stacked images, we can tell there is some continuum emission contamination evident on the upper left of both images. This shows that even with UVSUB and

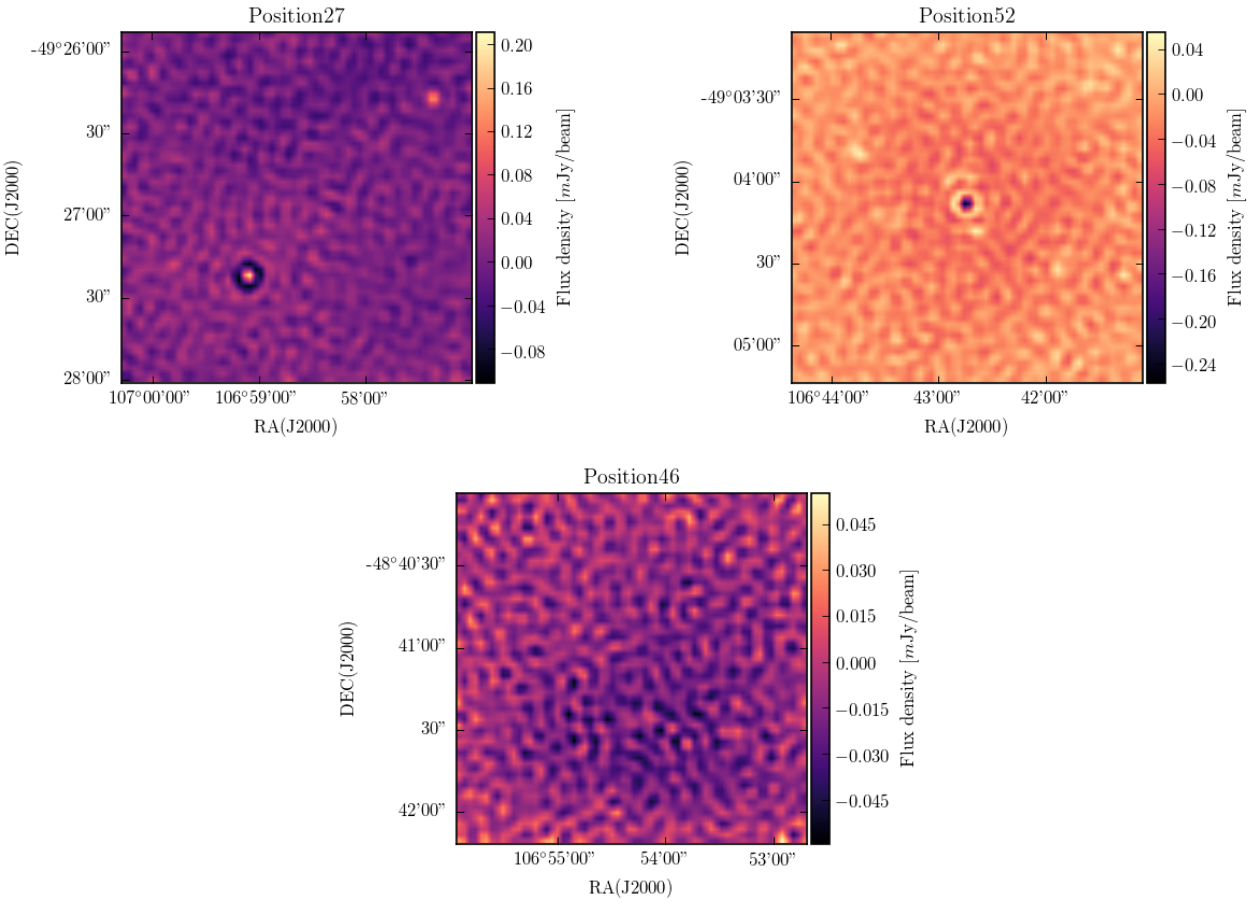

FIGURE 4.10: Examples of postage stamps from stacking positions for the non-detected (**top left panel**), non-contaminated (**top right panel**), and non-contaminated fields, non-detection (**bottom panel**) sub-samples.

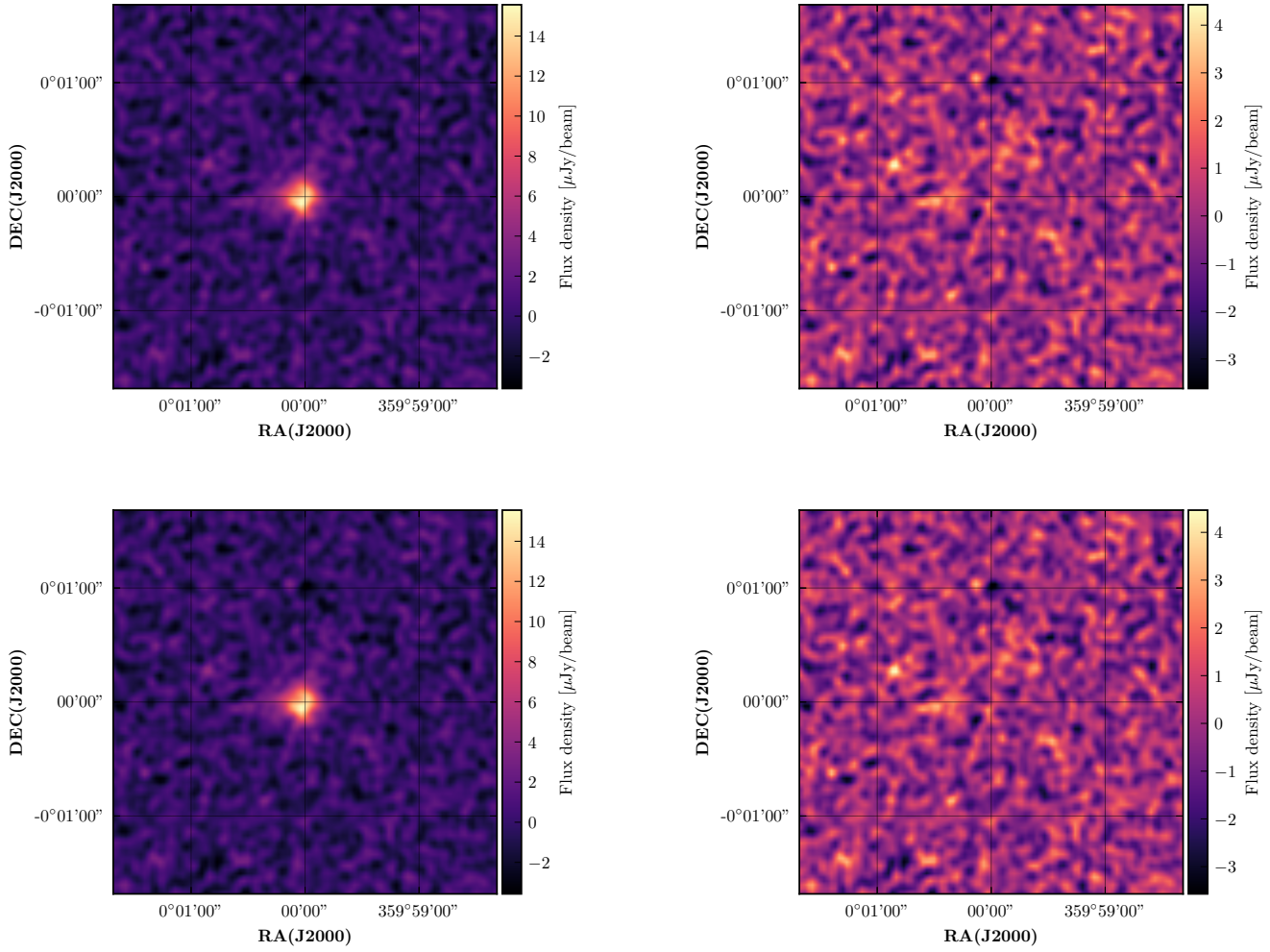

FIGURE 4.11: **Top left panel**: Mean stacked image for a full catalogue (dirty) and its residual map (**top right panel**). **Bottom left panel**: is the full catalogue (cleaned) stacked image and its residual map (**bottom right panel**). The dirty and cleaned maps (left column) are virtually indistinguishable. The residual images are made by subtracting a 2D Gaussian fit to the central detection from their corresponding stacked images; both residual maps show background Gaussian noise to a reasonable approximation. The results are of an ensemble of galaxies in the Abell 3408 galaxy cluster.

UVCONTSUB CASA continuum subtraction tasks, residual continuum may still be present that could bias results. Therefore, accurate deconvolution is important to limit this, which these images demonstrate.

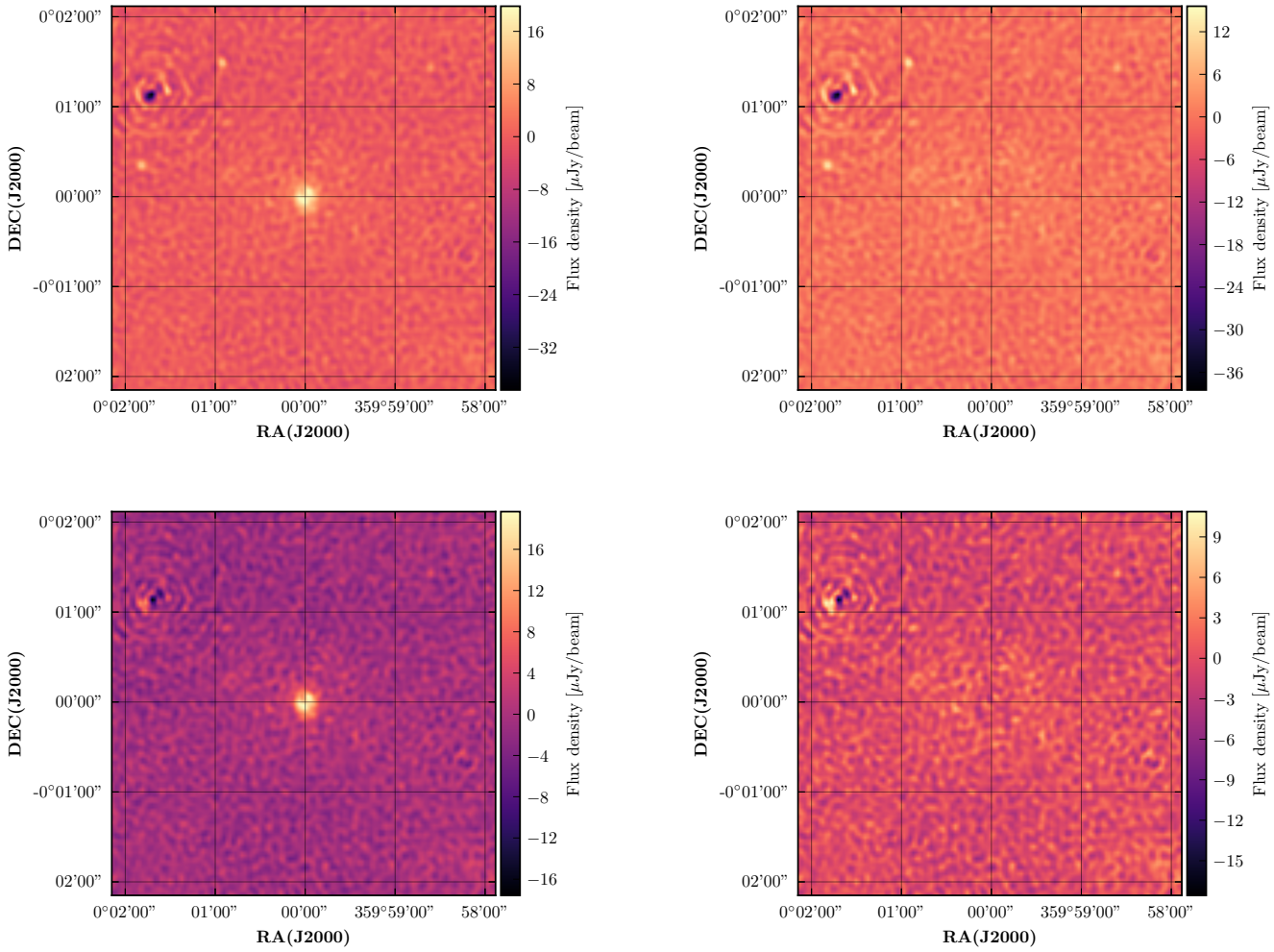

FIGURE 4.12: *uv*-stacking results on the ensemble of galaxies in the Abell 3408 galaxy cluster for a full catalogue (dirty) (**top panel**) and the full catalogue (cleaned) (**top panel**). From the right-hand side of each panel are corresponding residual images, made by subtracting a 2D Gaussian fit to the central stacked detection.

Figure 4.13 shows *uv*-stacking results for the three different sample catalogues: non-contaminated fields (top panel), non-detection fields (middle panel), and non-detect, non-contaminated (bottom panel). The *uv*-stacking procedure applied is similar to those discussed in Section 3.2.2, with remaining continuum emission subtracted out down to a clean flux density threshold of 10 μJy/beam, BRIGGS weighting with a robust parameter of -0.3. On the right-hand side of each panel are corresponding residual images made by subtracting a 2D Gaussian fit to the central stacked detection. The non-contaminated fields and non-detect, non-contaminated show similar peak flux density, while the non-detection fields having a lower peak flux density (shown on the colour scale) and also some off-centre detection on the upper left of the image.

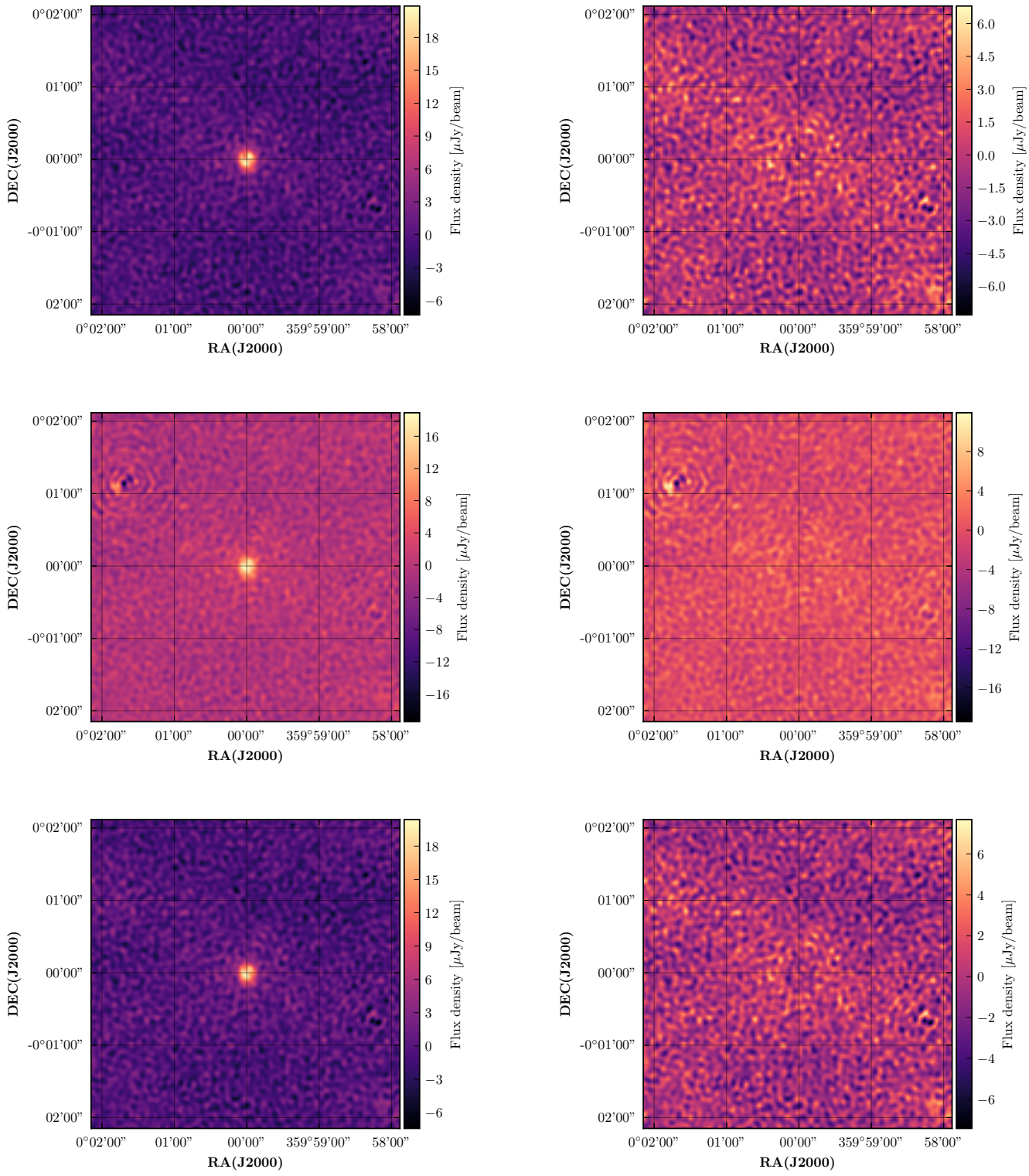

FIGURE 4.13: *uv*-stacking results on an ensemble of galaxies in the Abell 3408 galaxy cluster for three different sub-samples: non-contaminated fields (**top panel**), non-detection fields (**middle panel**), and non-contaminated fields and non-detect (**bottom panel**). The details of these sub-samples are explained in the main text. On the right-hand side are corresponding residual images made by subtracting a 2D Gaussian fit to the central detection.

Comparison of derived properties

Table 4.2 lists CASA task IMFIT results from image- and *uv*-stacked images. Shown are the fitted integrated flux density and geometric size for each stack, and the uncertainties are the fit error quoted by the `imfit` task. Figure 4.14 are uv-stacking results for the non-detected, non-contaminated sub-sample, fitting is done in the image-plane, but this is for illustration showing the stacked peak flux density. The typical average size of these galaxies is $\sim$ 6 arcsec which corresponds to a spatial scale 4.8 kpc at redshift $z = 0.04$. Figure 4.15 shows a plot of those results divided into image-stacking (black dots) and uv-stacking (red triangles). The image-stacking results have lower flux density compared to uv-stacking, this shows the robustness of the visibility stacking technique over the image-stacking method. Furthermore, on the right panel of Figure 4.15 is a plot of the measured brightness temperature T_b for the image- and *uv*-stacking results, the T_b is determined by applying the estimated integrated flux densities and geometric sizes into equation (4) and (5) in Condon et al., 1991, the figure shows that *uv*-stacking yields more accurate T_b values compared to image-stacking.

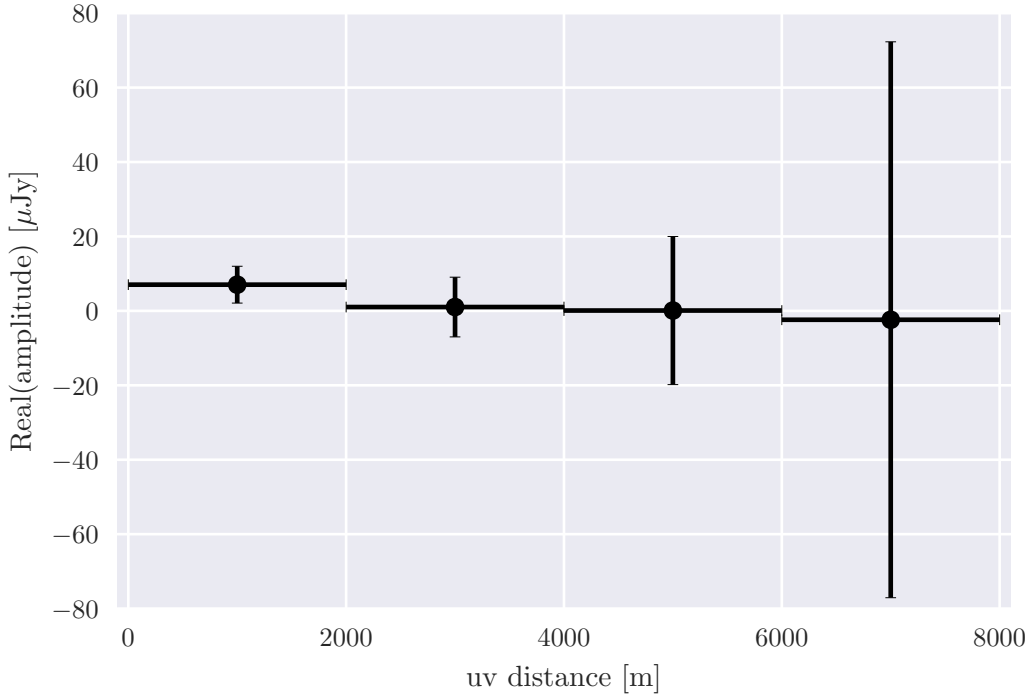

FIGURE 4.14: Stacked visibilities as a function *uv*-distance for a non-detect, non-contaminated sub-sample. The flux density is averaged *uv*-distance bins, taking the real part of the visibility amplitude. Uncertainties are defined as the standard deviation within each bin.

For uv-stacking, we can tell that the full catalogue (dirty and cleaned), non-contaminated fields and detection fields samples have produced superior stacking results. However, the results have contamination due to the remaining continuum emission. In this case, we are considering the non-detected, non-contaminated sub-sample as our best results, and also the stack has produced a relatively higher flux return compared the other samples.

TABLE 4.2: Comparison of stacking results on an ensemble of galaxies in the Abell 3408 galaxy cluster. Note that while the quoted integrated flux densities of $\gtrsim 100\ \mu\text{Jy beam}^{-1}$ might appear to be above the noise threshold, these are spatially-resolved stacked detections, and the peak flux densities are indeed below the detection threshold.

Sub-sample	**Image-stacking**		***uv*-stacking**	
	Integrated flux density (μJy)	Geometric size (arcsec)	Integrated flux density (μJy)	Geometric size (arcsec)
Full cat (dirty)	99.4 ± 7.57	5.98 ± 1.55	147 ± 13	5.64 ± 1.61
Full cat (cleaned)	99.5 ± 7.57	5.98 ± 1.55	148 ± 14	5.65 ± 1.60
Non-contaminated fields	90.8 ± 7.62	5.97 ± 1.62	150 ± 13	5.49 ± 1.61
Non-Detections	100.5 ± 7.58	5.98 ± 1.54	126 ± 12	5.54 ± 1.61
Non-detected, non-contaminated	93.8 ± 7.52	5.96 ± 1.58	137 ± 13	5.67 ± 1.63

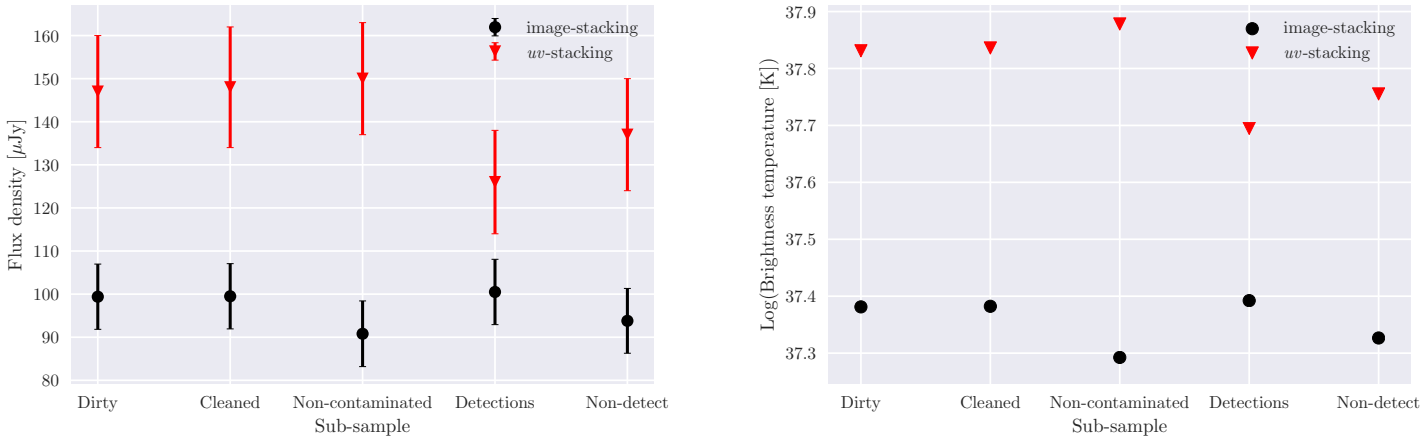

FIGURE 4.15: Measured integrated flux density (**left panel**) and brightness temperature (**right panel**) obtained from image- and *uv*-stacking, as shown on the legend the red triangles indicate data points from *uv*-stacking and the black dots data points are of image-stacking. The results are of an ensemble of galaxies in the Abell 3408 galaxy cluster, sub-samples used are listed on the x-axis of the plot. For each sub-sample, the integrated flux and geometric size is measured. The uncertainties for integrated flux are the fit error quoted by the `imfit` task.

4.2.1 Discussion

The stacking results presented show that *uv*-stacking appears to perform better compared to image-stacking. Image-stacking most likely suffer from CLEAN artefacts or correlated noise structure that are present in an image map before the stacking procedure, although image-stacking requires less computing time. We have found that when per*uv*-stacking on the full catalogue, there is some background emission that affects stacking results adversely, as seen more strongly for deep fields simulated in this thesis. This indicates that *uv*-stacking should be used with caution to obtain results with high flux and brightness temperature return. In our case, we solved this problem by splitting the full catalogue of 64 target sources into five subsample catalogues. From that, we can get better flux density and brightness temperature results, as shown in Table 4.2 and Figure 4.15.

As for the geometric size in Table 4.2 we were expecting the same to be more robust for *uv*-stacking compared to image-stacking, but the difference in results between the two is less than 1%, a result that will be interesting to explore with larger and more low-redshift samples. This thesis aims to demonstrate the difference between the two stacking methods, the systematic behind the geometric size results is beyond the scope of this thesis.

Placing these results on real data in a broader scientific context, it is important to note that Abell 3408 was also selected as one of an example of many $z \sim -0.05$ groups or clusters that MeerKAT seems particularly well suited at mapping. This has been seen in several early science examples with MeerKAT, from the Blecher et al. (in prep.) Abell 3408 work discussed and used in this chapter; as well as new, serendipitous discoveries of galaxy groups at a similar redshift (Lawrie et al., in prep.; Ranchod et al., in prep.). The systems all include several tens of HI galaxies and radio continuum sensitivities of order $\sim 10\,\mu$Jy beam^{-1}. Continuum stacking on these HI-selected objects will therefore enable an order of magnitude deeper probe of the SFR, taking the detection threshold down from $\gtrsim 0.1$ M$_\odot$ yr^{-1}, to $\gtrsim 0.01$ M$_\odot$ yr^{-1}. This is an important parameter space to probe, given the corresponding HI mass detection threshold is of order $M^*_{\rm HI}$ (i.e. $\gtrsim 10^9$ M$_\odot$), lowering the detection threshold is particularly important in measuring any putative star formation quenching in these rich cluster and group environments. Therefore, it is important to lower the SFR detection threshold to at least an order of magnitude below that of a Milky-Way-like galaxy on the SFR main sequence. Radial profiles of SFR are also important diagnostics of galaxy transformation in these environments, so the robustness of estimating aggregate sizes with visibility stacking may also play an important role in this scientific use case.

For all the computational expense and pitfalls associated with visibility stacking, this section shows a clear science application where it works with real MeerKAT, with benefits including improved integrated flux estimation and more robust size measurements, as well as derived quantities such as constraints to measure the aggregate star formation rates and brightness temperature constraints. All of this was with reasonable processing time and so we anticipate certain specialist science applications in the future.

Chapter 5

Conclusions and future directions

In this thesis, we explore the prospects of applying the visibility stacking technique to both simulated and real MeerKAT data. We find that there are a wide range of challenges to its successful implementation, owing to a broad range of attributes of MeerKAT and calibration. These include:

1. **Source Confusion:** Owing to MeerKAT's high sensitivity but moderate angular resolution, observations hit the confusion limit within $\sim$10 hours, greatly limiting stacking applications at these depths.
2. **Bright source contamination:** MeerKAT's high sensitivity and wide field-of-view also result in many bright sources ($\gtrsim 100mJy$ being observed within a single pointing, again limiting stacking experiments at low flux density levels, exacerbated by calibration and deconvolution errors, especially if these are noticeably direction-dependent.
3. **Computational expense:** visibility stacking with interferometers with many elements dramatically increases the processing time required for a given stacking experiment when compared with the image-plane stacking equivalent.

Despite the above challenges, we still demonstrate the successful use of visibility stacking on real MeerKAT dataset. This suggests that the techniques may be usefully applied in certain, high-scientific yield contexts. The requirements are that the observations are relatively shallow, and there is little impact from bright, extended, off-axis sources. This may therefore be applicable in high-value cases where a robust estimate of the aggregate size of the underlying population is important, or if multiple-component modelling of the aggregate population is desired.

However, on the whole, it is clear that visibility stacking is not as well suited in a MeerKAT sense for large populations of sources, as compared to ALMA or high-frequency VLA, for example. Nonetheless, we list below a set of systematic tests one could perform in the future to further explore the virtues of visibility stacking in a MeerKAT context.

1. Low-redshift HI stacking, specifically probing the angular size of marginally resolved, low-mass HI galaxies.
2. Annulus stacking of large nearby galaxies, where the column densities are below the detection threshold, however, velocity field models can predict the 3D coordinates of where diffuse HI may be.
3. The potential for certain fields to use facet calibration, and visibility stacking groups of unresolved sources in individual fields in order to boost SNR and enable self-calibration for that particular facet.

Despite the great sensitivity of the MeerKAT telescope, astronomers always have the desire to search deeper, so a broad range of statistical and stacking approaches will continue to be immensely valuable for a range of applications in the near and long term.

Appendix A

Software documentation summary

The following appendix serves as summary documentation for the use of the AUTOSTACKER module.

A.1 Prerequisites

AUTOSTACKER is publicly available and maintained on https://github.com/thatoeugine/AutoStacker.git. For bug reports, open an issue on github/submit a pull request. The module currently runs on the ILIFU[1] cluster and it is divided into simulation and stacking tools, which consists of software publicly available and maintained elsewhere:

Simulation tools

1. SIMUCLASS [2]
2. SIMMS[3]
3. MEQTREES[4]
4. WSCLEAN (Offringa et al., 2014)

Stacking tools

1. STACKER (Lindroos et al., 2014)
2. CASA[5]

A.2 Components

The module is divided into five main components namely:

1. simuclass: module for simulating radio interferometer observations, from sky model to deconvolved images, built in support of the SuperCLASS experiment: http://www.e-merlin.ac.uk/legacy/projects/superclass.html,
2. stackauto: a suite of code for simulating MeerKAT's observation and stacking MeerKAT data both image- and *uv*-plane,

[1] http://docs.ilifu.ac.za/#/
[2] https://bitbucket.org/itrharrison/simuclass
[3] https://github.com/SpheMakh/simms
[4] http://meqtrees.net/
[5] https://casa.nrao.edu/

3. fulltrecs.ini: configuration file for generating and stacking a large T-RECS sky model for a field of view of choice,
4. stackingdepth.ini: configuration file generating and stacking a small T-RECS sky model based on the stacking depth,
5. Mastercode.py: a master code that controls the entire module and doe not require any changes or edits.

A.3 Usage

We will first discuss the simple case of running AUTOSTACKER with the pre-written configuration files. To run in the AUTOSTACKER repository we pass the master code script and a configuration file to Python for e.g.,

```
python Mastercode.py stackingdepth.in
```

Depending on the command in the configuration file, the module will output different files, for a case of a full run of the configuration the files listed in Table A.1 will be the output:

TABLE A.1: A list and explanation of output files produced by the AUTOSTACKER module.

Name of output file	**Comment**
Measurement set (.ms)	simulated measurement set with noise added and *uv*-stacked measurement set
Sky Model catalogue (.txt)	A sample catalogue of SFGs from the Tiered Radio Extragalactic Continuum Simulation (T-RECS) catalogue by Bonaldi et al. (2018).
Sky Model image (.fits)	A model image consisting of sources from the sky model catalogue.
Stack positions (.csv)	Positions of the target sources.
Ground truth stacked image (.fits)	Median image stacked product of the sky model image (i.e., *uv*-sampling not applied).
uv-stacked image (.fits)	uv-stacked image.

A.3.1 Full T-RECS simulation plus stacking

For a case of running a full simulation plus stacking the *doskymodel*, *dosimulate* and *dosimulate* commands under the pipeline parameters of the configuration file should be switched ON, and also this can only be run using the full_trecs.ini configuration file. An example of such is shown here:

```
[pipeline]
doskymodel = True
dosimulate = True
dostacking = True
dosimdata = False
doimagedata = False
```

And also the *full_stack* command under the stacking parameters should also be switched ON, for e.g.,

```
[stacking_params]
full_stack =  True
stacking_depth = False
res_element_per_source = 100
im_noise_Jy = 5.54e-6
stacking_depth_skymodel_name = stack_auto/trecs-simu_truthcat.txt
FOV_size_cut = False
FOV_size_sqdeg = 0.84
FOV_size_cut_value = 0.5
No._of_srcs_of_choice = False
No._of_srcs = 10
flux_density_Jy = 1e-6
src_size_arcsec = 0
stack_clean = True
```

A.3.2 Stacking depth simulation plus stacking

For a case of running a stacking depth simulation plus stacking the *doskymodel*, *dosimulate* and *dosimulate* commands under the pipeline parameters of the configuration file should be switched ON, and also this can only be run using the stackingdepth.ini configuration file. An example of such is shown here:

```
[pipeline]
doskymodel = True
dosimulate = True
dostacking = True
dosimdata = False
doimagedata = False
```

And also either the *stacking_depth* or *No._of_srcs_of_choice* command under the stacking parameters should also be switched ON. For a case of stacking within a certain field of view, the *FOV_size_cut* should be ON and the size cut value and size of the observed field of view should be specified, for e.g.,

```
[stacking_params]
stacking_depth = False
res_element_per_source = 100
im_noise_Jy = 3e-6
stacking_depth_skymodel_name = stack_auto/trecs-simu_truthcat.txt
FOV_size_cut = False
FOV_size_sqdeg = 0.84
FOV_size_cut_value = 0.5
No._of_srcs_of_choice = True
No._of_srcs = 10
flux_density_Jy = 1e-6
src_size_arcsec = 0
stack_clean = True
```

A.3.3 Stacking-only usage

For both cases of either a full simulation or stacking depth, stacking can be run by switching only the *dostacking* command ON under the pipeline parameters in the configuration files, for e.g.,

```
[pipeline]
doskymodel = False
dosimulate = False
dostacking = True
dosimdata = False
doimagedata = False
```

An example of a fully documented .ini config file can be found here and the paramter files documentation can be found here https://github.com/thatoeugine/uv-stacking_MeerKAT_sim_data/wiki/params.json-Config-file-documentation, in a case where the default parameters need to be changed.

Bibliography

Antonucci, Robert (1993). "Unified models for active galactic nuclei and quasars". In: *Annual review of astronomy and astrophysics* 31, pp. 473–521.

Atemkeng, M. T. et al. (2016). "Using baseline-dependent window functions for data compression and field-of-interest shaping in radio interferometry". In: *Monthly Notices of the Royal Astronomical Society* 462.3, pp. 2542–2558. ISSN: 13652966. DOI: 10.1093/mnras/stw1656. arXiv: 1607.04106. URL: http://arxiv.org/abs/1607.04106http://dx.doi.org/10.1093/mnras/stw1656.

Barthel, Peter D (1989). "Is every quasar beamed?" In: *The Astrophysical Journal* 336, pp. 606–611.

Bell, Eric F (2003). "Estimating star formation rates from infrared and radio luminosities: the origin of the radio-infrared correlation". In: *The Astrophysical Journal* 586.2, p. 794.

Bera, Apurba et al. (2019). "Atomic Hydrogen in Star-forming Galaxies at Intermediate Redshifts". In: *The Astrophysical Journal* 882.1, p. L7. ISSN: 2041-8213. DOI: 10.3847/2041-8213/ab3656. arXiv: 1909.05905.

Boccardi, B. et al. (2017). "Radio observations of active galactic nuclei with mm-VLBI". In: DOI: 10.1007/s00159-017-0105-6. arXiv: 1711.07548. URL: http://arxiv.org/abs/1711.07548http://dx.doi.org/10.1007/s00159-017-0105-6.

Bonaldi, Anna and Robert Braun for the SKAO Science Team (2018). "Square Kilometre Array Science Data Challenge 1". In: pp. 1–7. arXiv: 1811.10454. URL: http://arxiv.org/abs/1811.10454.

Bonaldi, Anna et al. (2018). "The Tiered Radio Extragalactic Continuum Simulation (T-RECS)". In: *Monthly Notices of the Royal Astronomical Society* 482.1, pp. 2–19. ISSN: 13652966. DOI: 10.1093/mnras/sty2603. arXiv: 1805.05222. URL: http://arxiv.org/abs/1805.05222http://dx.doi.org/10.1093/mnras/sty2603.

Booth, Roy S and Justin Jonas (2009). "MeerKAT Key Project Science, Specifications, and Proposals". In: October. arXiv: arXiv:0910.2935v2.

Bouman, Katherine L. et al. (2016). "Computational Imaging for VLBI Image Reconstruction". In: *2016 IEEE Conference on Computer Vision and Pattern Recognition (CVPR)*, pp. 913–922. ISSN: 10636919. DOI: 10.1109/CVPR.2016.105. arXiv: 1512.01413. URL: http://ieeexplore.ieee.org/document/7780474/.

Bradt, Hale (2004). *Astronomy methods: A physical approach to astronomical observations*. Cambridge University Press.

Condon, JJ (1992). "Radio emission from normal galaxies". In: *Annual review of astronomy and astrophysics* 30.1, pp. 575–611.

Condon, J.J. and S.M. Ransom (2016). *Essential Radio Astronomy*. Princeton series in modern observational astronomy. Princeton University Press. ISBN: 9780691137797. URL: https://books.google.co.za/books?id=aY1VawEACAAJ.

Condon, JJ et al. (1991). "Compact starbursts in ultraluminous infrared galaxies". In: *The Astrophysical Journal* 378, pp. 65–76.

Cornwell, Tim J (2008). "Multiscale CLEAN deconvolution of radio synthesis images". In: *IEEE Journal of Selected Topics in Signal Processing* 2.5, pp. 793–801.

Davidsen, Arthur F et al. (1992). "The Hopkins Ultraviolet Telescope-Performance and calibration during the Astro-1 mission". In: *The Astrophysical Journal* 392, pp. 264–271.

Dunne, L. et al. (2009). "The star formation history of K-selected galaxies". In: *Monthly Notices of the Royal Astronomical Society* 394.1, pp. 3–20. ISSN: 00358711. DOI: 10.1111/j.1365-2966.2008.13900.x.

Fanson, James L et al. (1998). "Space infrared telescope facility (SIRTF)". In: *Space Telescopes and Instruments V*. Vol. 3356. International Society for Optics and Photonics, pp. 478–491.

Garn, Timothy and Paul Alexander (2008). "Radio source stacking and the infrared / radio correlation at microJy flux densities". In: 24.November, pp. 1–12. DOI: 10.1111/j.1365-2966.2008.14296.x. arXiv: 0812.0281. URL: http://arxiv.org/abs/0812.0281{\%}0Ahttp://dx.doi.org/10.1111/j.1365-2966.2008.14296.x.

— (2009). "Radio source stacking and the infrared/radio correlation at μjy flux densities". In: *Monthly Notices of the Royal Astronomical Society* 394.1, pp. 105–116. ISSN: 00358711. DOI: 10.1111/j.1365-2966.2008.14296.x.

Grobler, T. L. et al. (2014a). "Calibration artefacts in radio interferometry - I. ghost sources in westerbork synthesis radio telescope data". In: *Monthly Notices of the Royal Astronomical Society* 439.4, pp. 4030–4047. ISSN: 13652966. DOI: 10.1093/mnras/stu268.

Grobler, Trienko Lups et al. (2014b). "Calibration artefacts in radio interferometry–I. Ghost sources in Westerbork Synthesis Radio Telescope data". In: *Monthly Notices of the Royal Astronomical Society* 439.4, pp. 4030–4047.

Groves, Brent (2006). "The Narrow Line Region: Current Models and Future Questions". In: *The Central Engine of Active Galactic Nuclei, ASP Conference Series, Vol. 373, proceedings of the conference held 16-21 October, 2006 at Xi'an Jioatong University, Xi'an, China. Edited by Luis C. Ho and Jian-Min Wang, p.511* 373, p. 511. ISSN: 1050-3390. arXiv: 0612309 [astro-ph]. URL: http://arxiv.org/abs/astro-ph/0612309.

Gunn, James E and J Richard Gott (1972). "On the infall of matter into clusters of galaxies and some effects on their evolution". In: *The Astrophysical Journal* 176, p. 1.

Haarlem, Michael P van et al. (2013). "LOFAR: The low-frequency array". In: *Astronomy & astrophysics* 556, A2.

Hamaker, J. P., J. D. Bregman, and R. J. Sault (1996). "Understanding radio polarimetry. I. Mathematical foundations". In: *Astronomy and Astrophysics Supplement Series* 117.1, pp. 137–147. ISSN: 03650138. DOI: 10.1051/aas:1996146.

Heckman, Timothy M. and Philip N. Best (2014). "The Coevolution of Galaxies and Supermassive Black Holes: Insights from Surveys of the Contemporary Universe". In: *Annual Review of Astronomy and Astrophysics* 52.1, pp. 589–660. ISSN: 0066-4146. DOI: 10.1146/annurev-astro-081913-035722. arXiv: 1403.4620.

Heywood, I et al. (2019). "Inflation of 430-parsec bipolar radio bubbles in the Galactic Centre by an energetic event". In: *Nature* 573.7773, pp. 235–237.

Hogbom, JA and WN Brouw (1974). "The synthesis radio telescope at Westerbork. Principles of operation, performance and data reduction". In: *Astronomy and Astrophysics* 33, p. 289.

Hopkins, Andrew M and John F Beacom (2006). "On the normalization of the cosmic star formation history". In: *The Astrophysical Journal* 651.1, p. 142.

Jansky, Karl G (1933). "Electrical disturbances apparently of extraterrestrial origin". In: *Proceedings of the Institute of Radio Engineers* 21.10, pp. 1387–1398.

Jonas, Justin L. (2016). "The MeerKAT radio telescope". In: *Proceedings of Science*, pp. 25–27. ISSN: 18248039. DOI: 10.22323/1.277.0001.

Jonas, Justin L, Eddie E Baart, and George D Nicolson (1998). "The Rhodes/HartRAO 2326-MHz radio continuum survey". In: *Monthly Notices of the Royal Astronomical Society* 297.4, pp. 977–989.

King, A (2015). *Radiative Processes in Astrophysics*. Vol. 31. 10, pp. 359–359. ISBN: 9780471827597. DOI: 10.1088/0031-9112/31/10/053.

Knudsen, Kirsten K. et al. (2014). "Stacking of SKA data: Comparing uv-plane and image-plane stacking". In: *Proceedings of Science* 9-13-June-, pp. 1–8. ISSN: 18248039. arXiv: 1501.05643.

Lancaster, M (1989). *FUNDAMENTALS OF RADIO ASTRONOMY*. Vol. 53. March, pp. 1–30. ISBN: 9788578110796. DOI: 10.1017/CBO9781107415324.004. arXiv: arXiv:1011.1669v3. URL: http://ebooks.cambridge.org/ref/id/CBO9781107415324A009.

Lindroos, L. et al. (2014). "Stacking of large interferometric data sets in the image- and uv-domain - a comparative study". In: *Monthly Notices of the Royal Astronomical Society* 446.4, pp. 3502–3515. ISSN: 13652966. DOI: 10.1093/mnras/stu2344. arXiv: arXiv:1411.1410v1.

Lindroos, Lukas (2014). "Stacking of interferometric data at sub-millimeter and radio wavelengths Department of Earth and Space Sciences". In:

Madau, Piero and Mark Dickinson (2014). "Cosmic Star-Formation History". In: *Annual Review of Astronomy and Astrophysics* 52.1, pp. 415–486. ISSN: 0066-4146. DOI: 10.1146/annurev-astro-081811-125615. arXiv: 1403.0007.

Marr, Jonathan M, Ronald L Snell, and Stanley E Kurtz (2015). *Fundamentals of radio astronomy: observational methods*. CRC Press.

Mauch, T. et al. (2019). "The 1.28 GHz MeerKAT DEEP2 Image". In: 2014. arXiv: 1912.06212. URL: http://arxiv.org/abs/1912.06212.

Mauch, T et al. (2020). "The 1.28 ghz meerkat deep2 image". In: *The Astrophysical Journal* 888.2, p. 61.

Mitchell-Wynne, Ketron et al. (2014). "Beyond stacking: A maximum-likelihood method to constrain radio source counts below the detection threshold". In: *Monthly Notices of the Royal Astronomical Society* 437.3, pp. 2270–2278. ISSN: 00358711. DOI: 10.1093/mnras/stt2035.

Müller, Brigitte and Leo Peichl (1991). "Interferometry and Synthesis in Radio Astronomy 3rd ed". In: *Journal of Comparative Neurology* 308.1, pp. 91–102. ISSN: 10969861. DOI: 10.1002/cne.903080109.

Offringa, A. R. and O Smirnov (2017). "An optimized algorithm for multi-scale wide-band deconvolution of radio astronomical images". In: *Monthly Notices of the Royal Astronomical Society* 471.1, pp. 301–316. ISSN: 13652966. DOI: 10.1093/mnras/stx1547. arXiv: 1706.06786. URL: http://arxiv.org/abs/1706.06786http://dx.doi.org/10.1093/mnras/stx1547.

Offringa, A R et al. (2014). "WSClean : an implementation of a fast , generic wide-field imager for radio astronomy". In: 14.July, pp. 1–14. arXiv: arXiv:1407.1943v1.

Padovani, Paolo (2016). "The faint radio sky: radio astronomy becomes mainstream". In: *Astronomy and Astrophysics Review* 24.1. ISSN: 09354956. DOI: 10.1007/s00159-016-0098-6. arXiv: 1609.00499. URL: http://arxiv.org/abs/1609.00499http://dx.doi.org/10.1007/s00159-016-0098-6.

Popesso, P et al. (2019). "The main sequence of star-forming galaxies–I. The local relation and its bending". In: *Monthly Notices of the Royal Astronomical Society* 483.3, pp. 3213–3226.

Radcliffe, J. F. et al. (2016). "Multi-source self-calibration: Unveiling the microJy population of compact radio sources". In: *Astronomy and Astrophysics* 587. ISSN: 14320746. DOI: 10.1051/0004-6361/201527980. arXiv: 1601.04452.

Rau, Urvashi and Tim J Cornwell (2011). "A multi-scale multi-frequency deconvolution algorithm for synthesis imaging in radio interferometry". In: *Astronomy & Astrophysics* 532, A71.

Ryle, Martin and Anthony Hewish (1960). "The synthesis of large radio telescopes". In: *Monthly Notices of the Royal Astronomical Society* 120.3, pp. 220–230.

Sandage, Allan (1965). "The Existence of a Major New Constituent of the Universe: the Quasistellar Galaxies." In: *The Astrophysical Journal* 141, p. 1560.

Serra, Paolo et al. (2012). "The ATLAS3D project–XIII. Mass and morphology of H i in early-type galaxies as a function of environment". In: *Monthly Notices of the Royal Astronomical Society* 422.3, pp. 1835–1862.

Serra, Paolo et al. (2015). "SOFIA: A flexible source finder for 3D spectral line data". In: *Monthly Notices of the Royal Astronomical Society* 448.2, pp. 1922–1929. ISSN: 13652966. DOI: 10.1093/mnras/stv079. arXiv: 1501.03906.

Smirnov, Oleg M (2011). "Revisiting the radio interferometer measurement equation. I. A full-sky Jones formalism". In: 16082. DOI: 10.1051/0004-6361/201016082. arXiv: 1101.1764. URL: http://arxiv.org/abs/1101.1764http://dx.doi.org/10.1051/0004-6361/201016082.

Thompson, A Richard (1999). "Fundamentals of radio interferometry". In: *Synthesis Imaging in Radio Astronomy II*. Vol. 180, p. 11.

Véron-Cetty, M. P. and P. Véron (2000). "The emission line spectrum of active galactic nuclei and the unifying scheme". In: *Astronomy and Astrophysics Review* 10.1-2, pp. 81–133. ISSN: 09354956. DOI: 10.1007/s001590000006.

Wakker, BP and UJ Schwarz (1988). "The Multi-Resolution CLEAN and its application to the short-spacing problem in interferometry". In: *Astronomy and Astrophysics* 200, pp. 312–322.

Walker, Gordon (1987). *Astronomical observations: an optical perspective*. Cambridge University Press.

White, Richard L et al. (2006). "White et al. - 2007 - Signals from the Noise Image Stacking for Quasars in the FIRST Survey". In: pp. 1–16. URL: papers3://publication/uuid/DD5BB0FF-BF3C-4DFE-8BAE-24258135DECC.

Wilson, Andrew S. and Edward J. M. Colbert (1994). "The Difference between Radio-Loud and Radio-Quiet Active Galaxies". In: *The Astrophysical Journal* 438, p. 62. ISSN: 0004-637X. DOI: 10.1086/175054. arXiv: 9408005 [astro-ph]. URL: http://arxiv.org/abs/astro-ph/9408005http://dx.doi.org/10.1086/175054.

Wootten, Alwyn (2003). "The Atacama large millimeter array (ALMA)". In: *Large Ground-based Telescopes*. Vol. 4837. International Society for Optics and Photonics, pp. 110–118.

Wright, Andrew (2002). "Single-dish Radio Astronomy". In: Storey.

Xu, Chun, Mario Livio, and Stefi A. Baum (1999). "Radio Loud and Radio Quiet Active Galactic Nuclei". In: *The Astronomical Journal* 118.3, pp. 1169–1176. ISSN: 00046256. DOI: 10.1086/301007. arXiv: 9905322 [astro-ph]. URL: http://arxiv.org/abs/astro-ph/9905322http://dx.doi.org/10.1086/301007.

Zwart, Jonathan T.L. et al. (2014). "The star formation history of mass-selected galaxies from the VIDEO survey". In: *Monthly Notices of the Royal Astronomical Society* 439.2, pp. 1459–1471. ISSN: 13652966. DOI: 10.1093/mnras/stu053. arXiv: arXiv:1401.1648v1.